Supplementary Information

A dynamically phase-adaptive regulating hydrogel promotes ultrafast anti-fibrotic wound healing

Fan Zhang[1,2,3]†, Haijuan Zhang[1,2]†, Shengfu Wang[1,2], Mingying Gao[1,2], Kaiyi Du[2], Xinyuan Chen[2], Yang Lu[2], Qianqian Hu[2], Anyu Du[2], Shenghu Du[1], Jian Wang[1], Keqing Shi[1], Zimiao Chen[1], Zhuo Li[4*], Zhenglin Li[1,2,5*], Jian Xiao[1,2,3*]*

[1]Department of Wound healing, The First Affiliated Hospital of Wenzhou Medical University, Wenzhou, Zhejiang 325035, China.

[2]Oujiang Laboratory (Zhejiang Lab for Regenerative Medicine, Vision and Brain Health), School of Pharmaceutical Sciences, Wenzhou Medical University, Wenzhou, Zhejiang 325035, China.

[3]Wenzhou Institute, University of Chinese Academy of Sciences, Wenzhou, Zhejiang, 325001, China.

[4]Key Laboratory of Functional Inorganic Materials Chemistry (Ministry of Education), School of Chemistry and Materials Science, Heilongjiang University, Harbin, 150080, P. R. China.

[5]Cixi Biomedical Research Institute, Wenzhou Medical University, Wenzhou, Zhejiang 325035, China.

[*]Corresponding author. Email: gaomingying910108@163.com (M.Y.G.); lizhuo9410@hlju.edu.cn (Z.L.); chmlzh@wmu.edu.cn (Z.L.L.); xfxj2000@126.com (J.X.)

†These authors contributed equally to this work.

This PDF file includes:

Supplementary Methods

Supplementary Figures 1–54

Supplementary Tables 1–5

Supplementary Methods

Materials

$Ce(NO_3)_3 \cdot 6H_2O$ (99.95%), Oleylamine, 1-Octadecene (ODE), ε-poly-L-lysine • HCl (εPL), $NaIO_4$, Methanol and Ethanol were purchased from Aladdin Biochemical Technology Co., Ltd. (Shanghai, China). Sodium hyaluronate (HA) was purchased from Yuanye Biotechnology Co., Ltd. (Shanghai, China). *c-Jun* siRNA (the sense strand: GGCUACAGUAACCCUAAGATT, the antisense strand: UCUUAGGGUUACUGUAGCCTT) was purchased from GenePharma Co.,Ltd. (Shanghai, China), LB Broth, PBS, Modified Hematoxylin-Eosin Stain Kit and Masson's Trichrome Stain Kit were purchased from Solarbio Science & Technology Co., Ltd. (Beijing, China). Resomer® RG 504 H, Poly(D,L-lactide-co-glycolide) (50:50, Mw 38,000-54,000, 719900) and lipopolysaccharide (LPS) were purchased from Sigma-Aldrich (MO, USA). The bFGF was produced by Key Laboratory of Biotechnology and Pharmaceutical Engineering of Zhejiang Province, Wenzhou Medical University.

Property test of F/R gel

The rheological properties were measured by using a rheometer (HAAKE MARS60, Thermo Scientific) with 20 mm parallel plate geometry at 25 °C. For gel-forming kinetics, oscillatory time sweeps were performed at 1 Hz and 0.1% strain. Amplitude sweeps were carried out in the strain range of 0.1–1000% at 1 Hz to determine the breaking strains of the hydrogel.

The self-healing performance of hydrogel was evaluated macroscopically. In short, a blade was used to cut the hydrogel (shaped into a pentagram in advance) into three pieces. Then, the hydrogel was reassembled and allowed for self-healing for 30 min without additional interference. The healed gel's integrality was demonstrated by either stretching or immersing in PBS solution (pH = 7.4). To further investigate self-healing behaviors of the hydrogel, dynamical oscillatory strain amplitude sweep tests were also carried out at 1 Hz with alternate strain change between 1% for 120 s and 800% for 120 s, and a time-dependent modulus was observed.

The hydrogel's ductility was tested by stretching with tweezers. The adhesion

measurement was performed using the lap shear test with the INSTRON tensile tester at a rate of 20 mm/min. Hydrogel samples were sandwiched in between two pieces of fresh pig skin. By stretching the pig skins until the cohesion/adhesion of the gel failed, we would get the maximum tensile forces.

Component releasing experiments of F/R gel

1 mL of the F/R gel was placed in a 6-well plate supplemented with 3 ml of phosphate buffer solution (PBS, pH 4.5). The plate was then incubated at 37 °C in the dark. Releasing solutions were collected at predetermined time points. The concentration of εPL-CeO_v was measured using UV-vis spectrophotometer, while the released bFGF was determined by Enzyme-Linked Immunosorbent Assay (ELISA) Kit and c-Jun siRNA was measured using NanoDrop Microvolume Spectrophotometers (Thermo Scientific™ NanoDrop™ One).

Antibacterial experiments of the F/R gel

To evaluate the antibacterial ability, *E. coli* (ATCC25922), *S. aureus* (ATCC6538) or *MRSA* (ATCC43300) (1×10^8 CFU/mL) was incubated with LB Broth (Control) or the sample groups (CIP, εPL-CeO_v, F/R MCs, Gel and F/R gel) for 12 h at 37 ℃. Then, 10 μL of the bacteria solutions were diluted by 1×10^4 times, followed by spread on the LB agar plates. After 24 h, bacterial colonies were recorded and counted. Also, live/dead bacteria double staining assay (SYTO 9/PI, Keygen/Beyotime) was performed and observed by laser confocal microscopy.

The F/R gel's ability of inhibiting biofilm formation was then assessed. Firstly, E. coli, S. aureus and MRSA culture (1 mL, 1×10^8 CFU/mL) were added into a 24-well plate, respectively. After incubated at 37 °C without shaking for 6 h, the medium was replaced with fresh LB culture or LB containing material samples (CIP, εPL-CeO_v, F/R MCs, Gel and F/R gel), and then incubated at 37 °C for another 48 h without shaking. The biofilm in each group was washed with 0.9% NaCl, and stained with crystal violet. Following repeated wash by 0.9% NaCl, the biofilms were air-dried and photographed. The corresponding inhibition rate was calculated by dissolving biofilms in ethanol and measuring the OD570 nm values. To evaluate the F/R gel's efficiency of destructing mature biofilm, bacterial suspension was cultured in LB medium for 48 h to form

biofilms firstly, and then treated with blank LB culture medium (Control), CIP, εPL-CeOv, F/R MCs, Gel and F/R gel for another 12 h, respectively. The residual biofilms were also assessed using crystal violet staining. Besides, biofilms formed on the glass slides were treated with the above samples, and then stained with SYTO 9 and PI for 30 min in the dark, followed by observation under laser confocal microscopy.

Tube formation experiment of the F/R gel

HUVECs were seeded into 6-well plates at a density of 5×10^5 cells/well. After 24 hours of incubation, different samples (F/R MCs, Gel, F gel, and F/R gel) were added to the wells and incubated for an additional 24 hours. The cells were then treated with 100 μM tBHP for 4 hours at 37°C. Afterward, the cells were seeded into 48-well plates pre-coated with matrix gel at a density of 2×10^5 cells/well and cultured for 6 hours. Finally, the cells were stained with Calcium AM and observed under a fluorescence microscope.

Biocompatibility study of the F/R gel

Fresh red blood cells (RBCs) were obtained from C57BL/6 mice, and diluted by normal saline. Then, 1 mL RBCs suspension was mixed with 1 mL normal saline (negative control), distilled water (positive control) and sample groups (F/R MCs, Gel and F/R gel), which were preheated at 37 ℃ for 30 min. The mixtures were further incubated for 1 h at 37 ℃, then dripped onto a blood smear, and observed using an inverted microscope to assess the integrity of blood cells. The rest of mixed solutions were centrifugated (3000 rpm, 5 min), and the supernatants were carefully collected for $OD_{545\ nm}$ measurement. The hemolysis ratio was calculated by this calculation formula: Hemolysis (%) = $[OD_{sample}-OD_{negative\ control}] / [OD_{positive\ control}-OD_{negative\ control}] \times100\%$.

Three different cell lines were cultivated and used for the cytocompatibility experiments: 3T3 cell, HUVEC and C2C12 (5×10^4 cells) were cultured in a 24-well plate and incubated at 37 °C for 24 h. Then, the old medium was replaced with the fresh medium (Control) or the samples (F/R MCs, Gel and F/R gel), followed by continuous incubation at 37 °C for 24, 48, and 72 h, respectively. After the culture solution was replaced with the WST-8 reagent for 1 h at 37 °C, the cell plate's absorbance at 450 nm was detected by microplate reader. Meanwhile, live/dead cell staining assay was also carried out to evaluate the cytocompatibility of F/R gel.

***In vivo* biocompatibility evaluation of the F/R gel**

The F/R gel's in vivo biocompatibility was studied on mice (C57BL/6, male). In detail, the mice were dehaired and treated with the F/R gel on the back for 28 days. Bare healthy skin was selected as control group. The skin tissues and vital organs were collected and stored in 4% paraformaldehyde for H&E staining. In addition, the mouse blood samples were also collected for blood routine and blood biochemical tests.

The Retention capacity of εPL-CeO_v and MCs at wound site

εPL-CeO_v was successfully labeled with Cy5.5-NHS (εPL-CeO_v-Cy5.5), and a fluorescent gel (Gel (εPL-CeO_v-Cy5.5)) was then prepared using εPL-CeO_v-Cy5.5. Subsequently, In Vivo Imaging System was performed to observe the retention of εPL-CeO_v-Cy5.5 or Gel (εPL-CeO_v-Cy5.5) at the wound site. Consistent with previous methods, the retention of PLGA MCs-Cy5.5 or Gel (PLGA MCs-Cy5.5) at the wound site was monitored using In Vivo Imaging System.

Fluorescence-activated cell sorting (FACS) experiment of mouse wound tissues

In order to isolate individual cells from collected mouse skin tissues (n = 3) for FACS, a cell suspension needs to be prepared. Firstly, fresh skin samples were rinsed with PBS, then the samples were clipped with sterile curved scissors. Next, Hanks Buffered Salt Solution (HBSS) containing collagenase IV (1500 U/ml) was added to the tissue homogenate and incubated at 37 °C for 1 h, followed by neutralization with FACS buffer (containing 2% Fetal Bovine Serum and 1% penicillin-streptomycin). The homogenate obtained was filtered through 70 μm Nylon filter and centrifuged (200 g, 5 min, 4 ℃). Red Blood Cell Lysis Buffer was added within the homogenate precipitate obtained and incubated for 3 min. Then centrifuged (450 g, 5 min, 4 ℃) and resuspended with FACS buffer. Primary antibody (Ter119-Pacific Blue, CD45-PB, CD31-PB, CD324-Biotin, CD202b-Biotin, CD326-eFluor450, CD26-PerCPCy5.5, PDGFRα(CD140a)-PE-Cy7, Sca-1(Ly-6A/E)-BV605, PDGFRα-PE-Cy7, and DLK1-Allophycocyanin) staining was then performed for 30 min at 4 ℃, followed by centrifugation (450 g, 5 min, 4 ℃), washing of the cell suspension, and staining with secondary antibody (Streptavidin-eFluor450) for 20 min at 4 ℃. After staining, the excess antibody was washed, dead cells were labeled by DAPI, and diluted in 1 ml

FACS buffer. Finally, prepared cell samples were used for FACS (CytoFlex LX, Beckman Coulter). Information on the antibodies used in this experiment was shown in Table S3, and information on the remaining reagents was shown in Table S4.

Transcriptome sequencing and data analysis

The wound tissues of mice in Control group and F/R gel group were collected on day 14, respectively. After washed with saline, the tissues were stored at -80 °C before sequencing. Differential expression analysis of two conditions/ groups (three biological replicates per condition) was performed using the DESeq2 R package (1.20.0). Gene Ontology (GO) enrichment analysis of differentially expressed genes was implemented by the clusterProfiler R package (3.8.1), in which gene length bias was corrected. GO terms with corrected P value less than 0. 05 were considered significantly enriched by differential expressed genes. And we used clusterProfiler R package (3.8.1) to test the statistical enrichment of differential expression genes in KEGG pathways.

Supplementary Figures

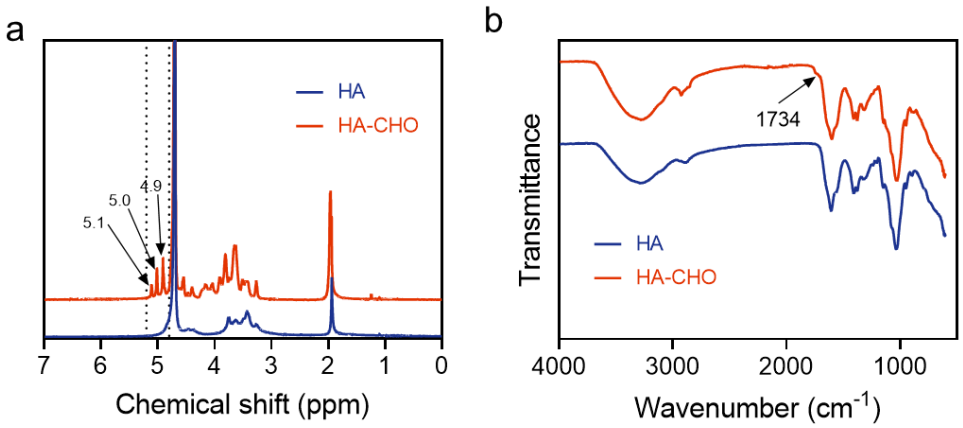

Supplementary Figure 1. Characterization of HA-CHO. (a) NMR spectroscopy. (b) Infrared spectroscopy.

Nuclear magnetic resonance (NMR) spectroscopy analysis showed three distinct peaks at 4.9 to 5.1 ppm, indicating the presence of protons associated with aldehyde groups. Fourier transform infrared (FTIR) spectroscopy revealed the emergence of a novel C=O stretching peak within the range of 1720-1751 cm^{-1}, which was attributed to the presence of aldehyde groups.

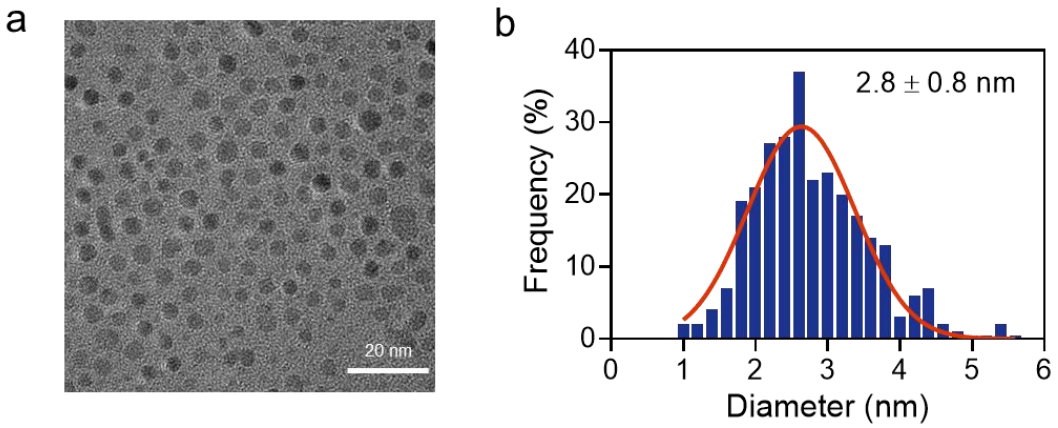

Supplementary Figure 2. Characterization of CeOv. (a) TEM image of the CeO_v nanoparticles. (b) Statistical distribution of the particle size. Three independent experiments were performed and representative results are shown in (a).

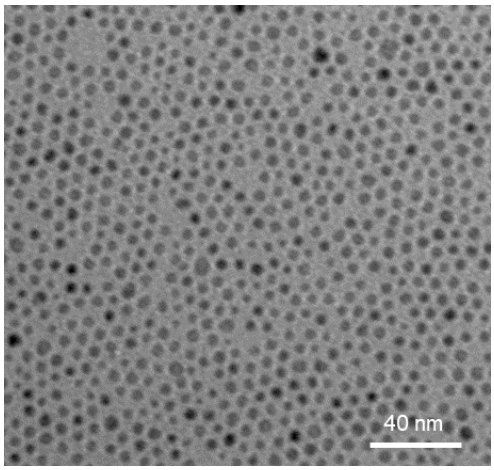

Supplementary Figure 3. TEM image of the εPL-CeO_v nanoparticles. No obvious size/morphology changes were found after εPL modification. Three independent experiments were performed and representative results are shown.

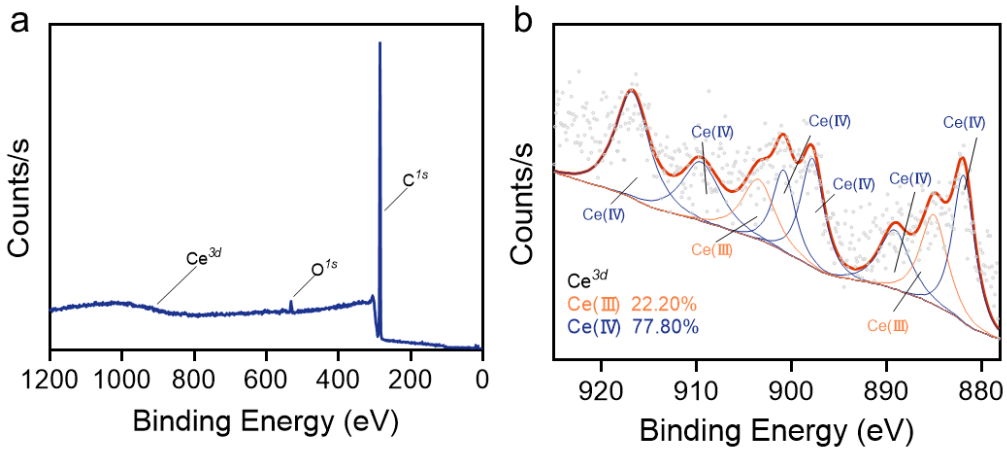

Supplementary Figure 4. XPS characterization of the CeO_v nanoparticles. (a) XPS result of CeO_v. (b) Ce^{3d} spectrum of CeO_v. Ce^{3+}/Ce^{4+} ratio was determined as about 22:78.

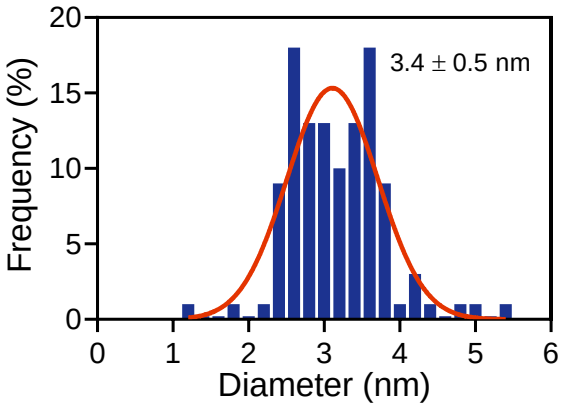

Supplementary Figure 5. Particle size distribution of the εPL-CeO_v nanoparticles by DLS. The nanoparticles had an average hydrodynamic size of ~ 3.4 ± 0.5 nm and a positive zeta potential of ~ 19.2 ± 1.4 mV.

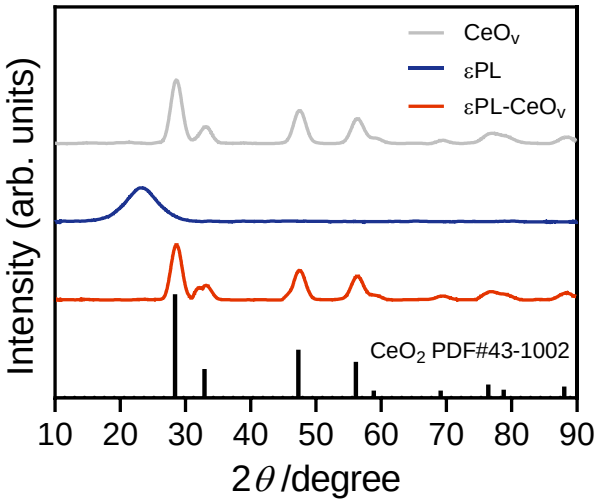

Supplementary Figure 6. XRD characterization.

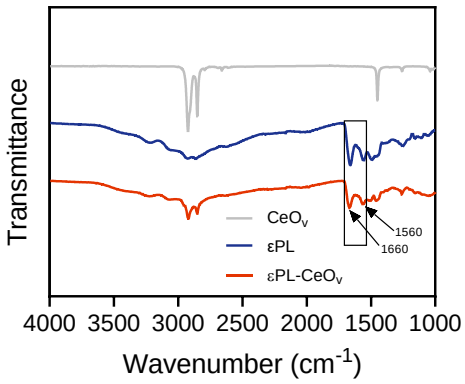

Supplementary Figure 7. Infrared spectroscopy of the CeO_v, εPL and εPL-CeO_v.

FTIR spectra revealed the characteristic peaks of amide I band at 1660 cm^{-1} and amide II band at 1560 cm^{-1} derived from εPL structure, indicating the successful synthesis of εPL-CeO_v nanoparticles.

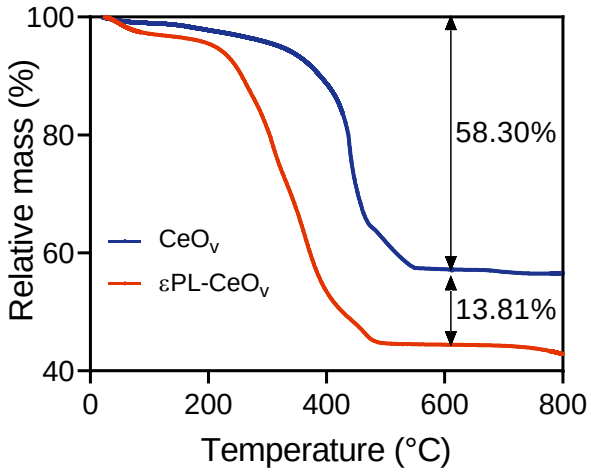

Supplementary Figure 8. Thermogravimetric analysis characterization of CeO_v sample before and after εPL modification. The amount of anchored εPL on CeO_v surface was ~ 13.8%.

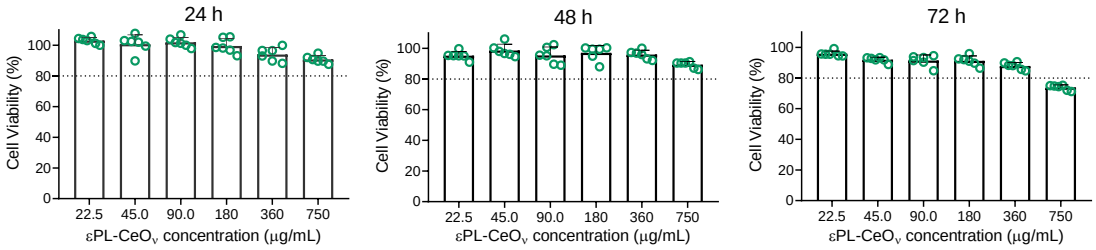

Supplementary Figure 9. Effect of different concentrations of εPL-CeO_v on cell viability by CCK-8 method (n = 6 independent samples). Data are presented as mean ± SD.

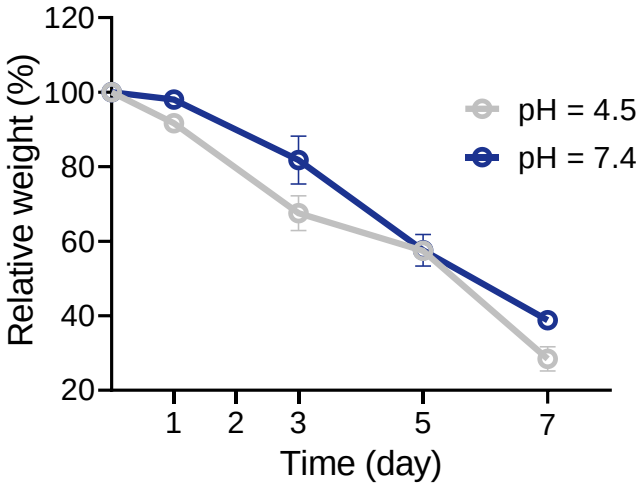

Supplementary Figure 10. *In vitro* degradation of PLGA microspheres. n = 3 independent samples, and data are presented as mean ± SD.

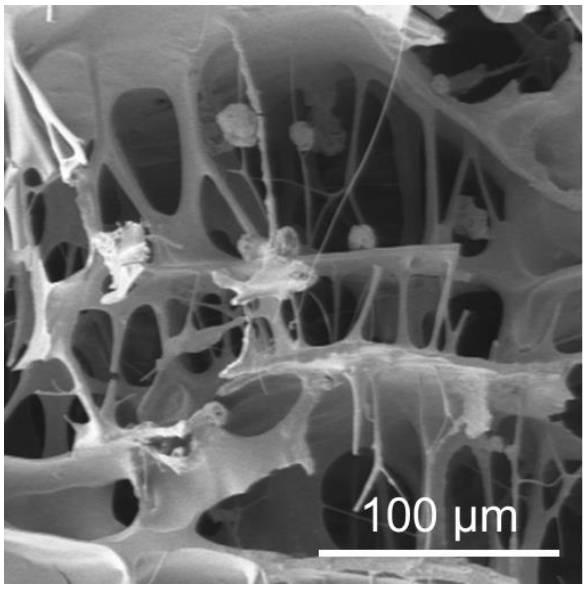

Supplementary Figure 11. SEM images of F/R gels. Three independent experiments were performed and representative results are shown.

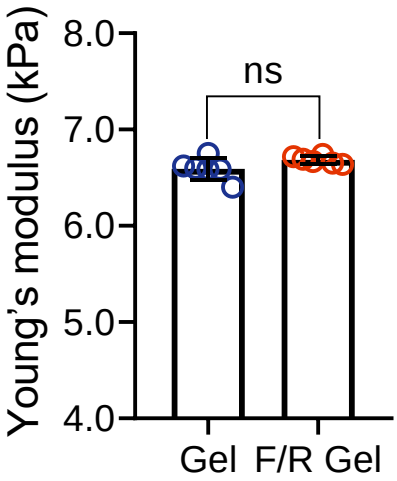

Supplementary Figure 12. Young's modulus of the Gel and F/R gel. n = 3 independent samples, and data are presented as mean ± SD.

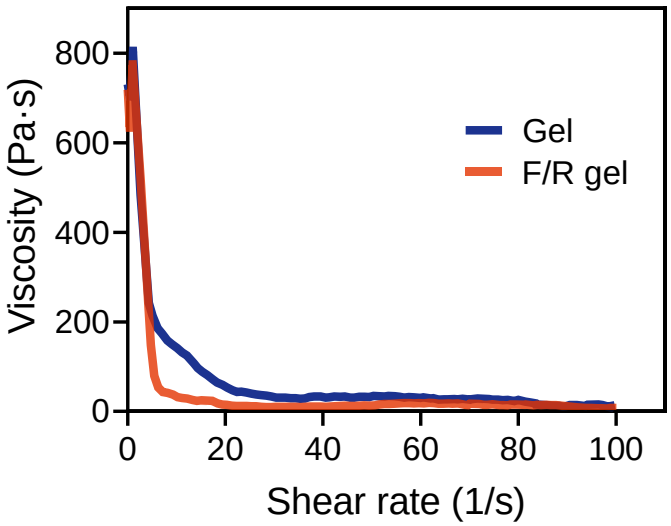

Supplementary Figure 13. Viscosity of the Gel and F/R gel.

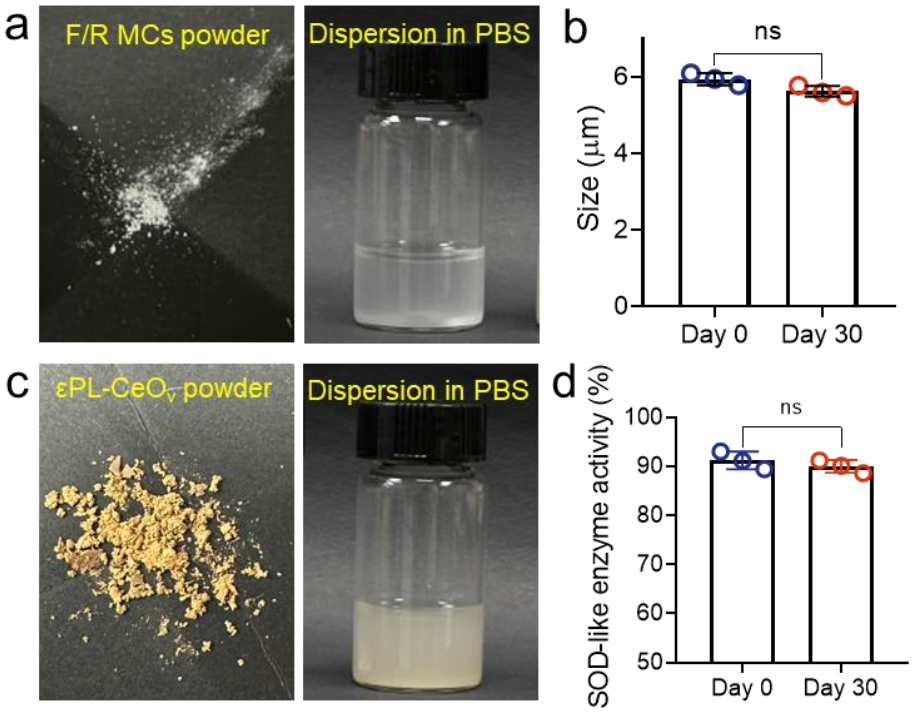

Supplementary Figure 14. The stability of F/R MCs and εPL-CeO_v. (a) Appearance and (b) Particle size of F/R MCs after 30 days (n = 3 independent samples). (c) Appearance and (d) SOD enzyme activity of εPL-CeO_v after 30 days (n = 3 independent samples). Data are presented as mean ± SD.

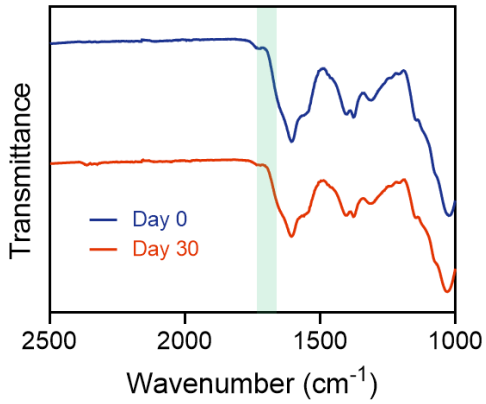

Supplementary Figure 15. Infrared spectroscopy of the HA-CHO after 30 days.

Supplementary Figure 16. Representative photographs of F/R gel adhesion in different states of different types of wounds. Three independent experiments were performed and representative results are shown.

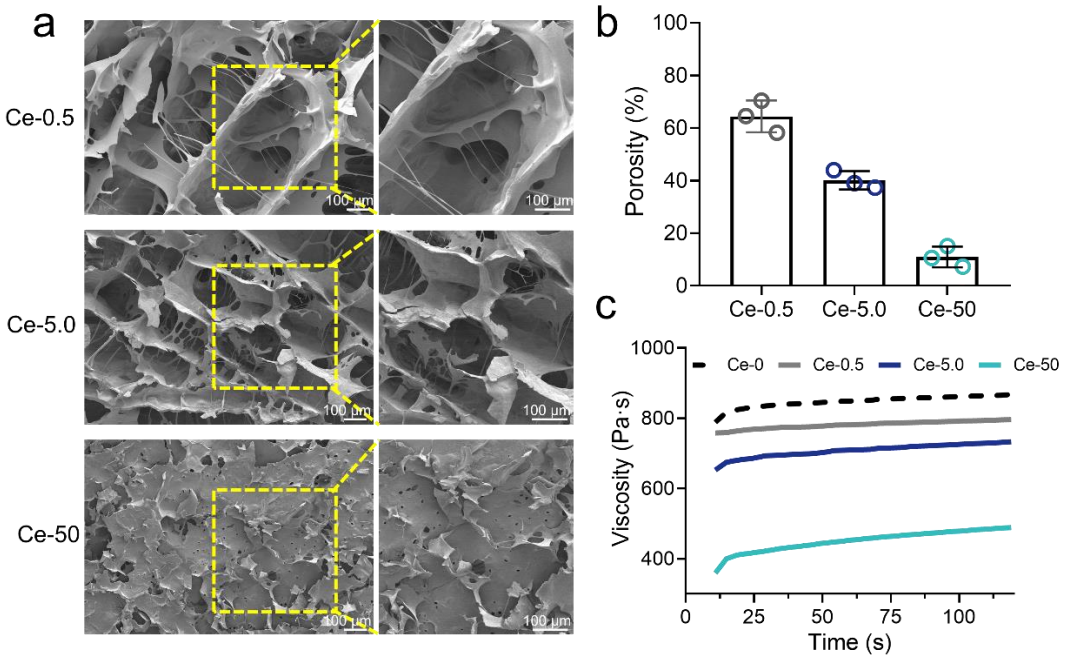

Supplementary Figure 17. Characterization of hydrogels with different concentrations of εPL-CeO_v. (a) SEM, (b) The porosity and (c) The viscosity. (n = 3 independent samples). Three independent experiments were performed and representative results are shown in (a). Data are presented as mean ± SD.

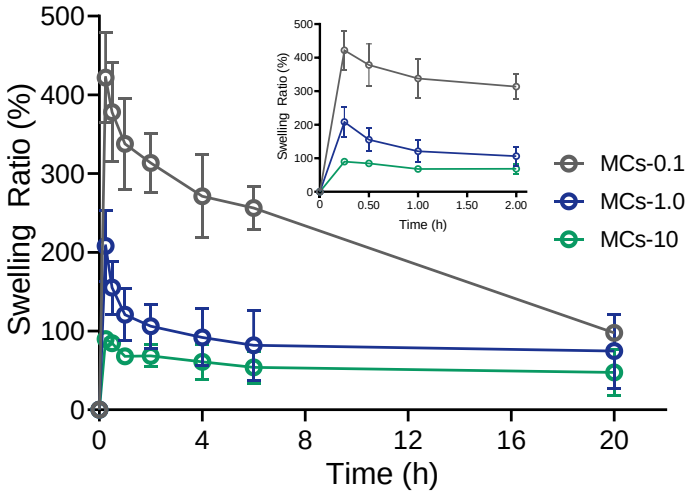

Supplementary Figure 18. The swelling ratio of hydrogels with different concentrations of MCs. n = 3 independent samples, and data are presented as mean ± SD.

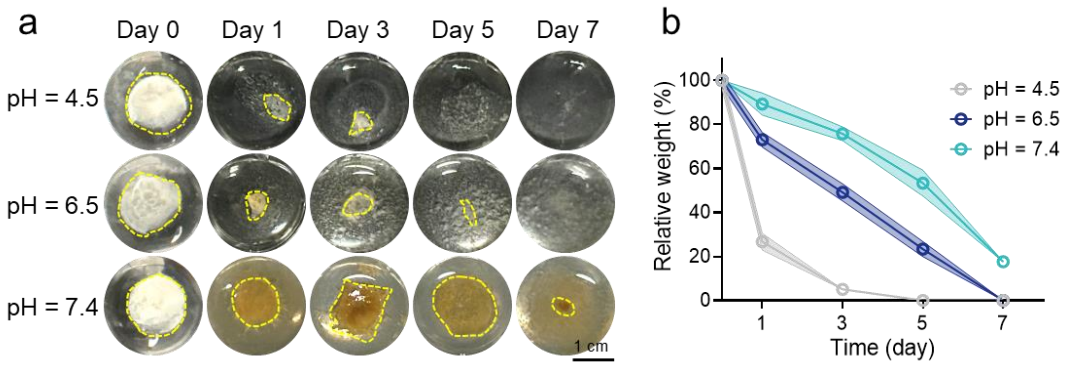

Supplementary Figure 19. *In vitro* Degradation Properties of F/R gel. (a) Representative photographs showing F/R gel morphology changes after incubated with pH = 4.5, pH = 6.5, or pH = 7.4 PBS. (b) The corresponding weight changes of F/R gel during the 7-day degradation process (n = 3 independent samples). Three independent experiments were performed and representative results are shown in (a). Data are presented as mean ± SD.

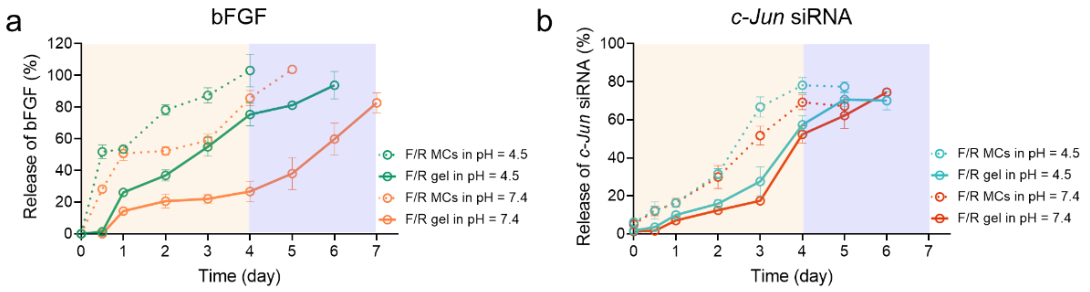

Supplementary Figure 20. *In vitro* release properties of (a) bFGF and (b) *c-Jun* siRNA from F/R MCs and F/R gel (n = 3 independent samples). Data are presented as mean ± SD.

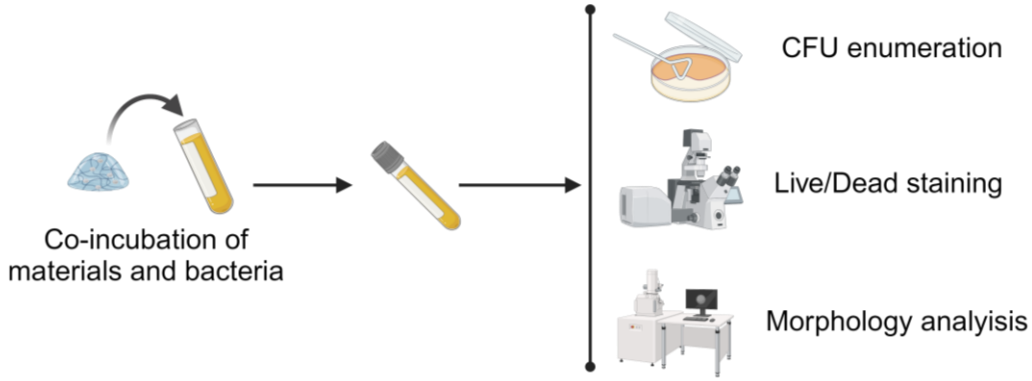

Supplementary Figure 21. Experimental illustration for the F/R gel's bacterial inhibition test (created with BioRender.com).

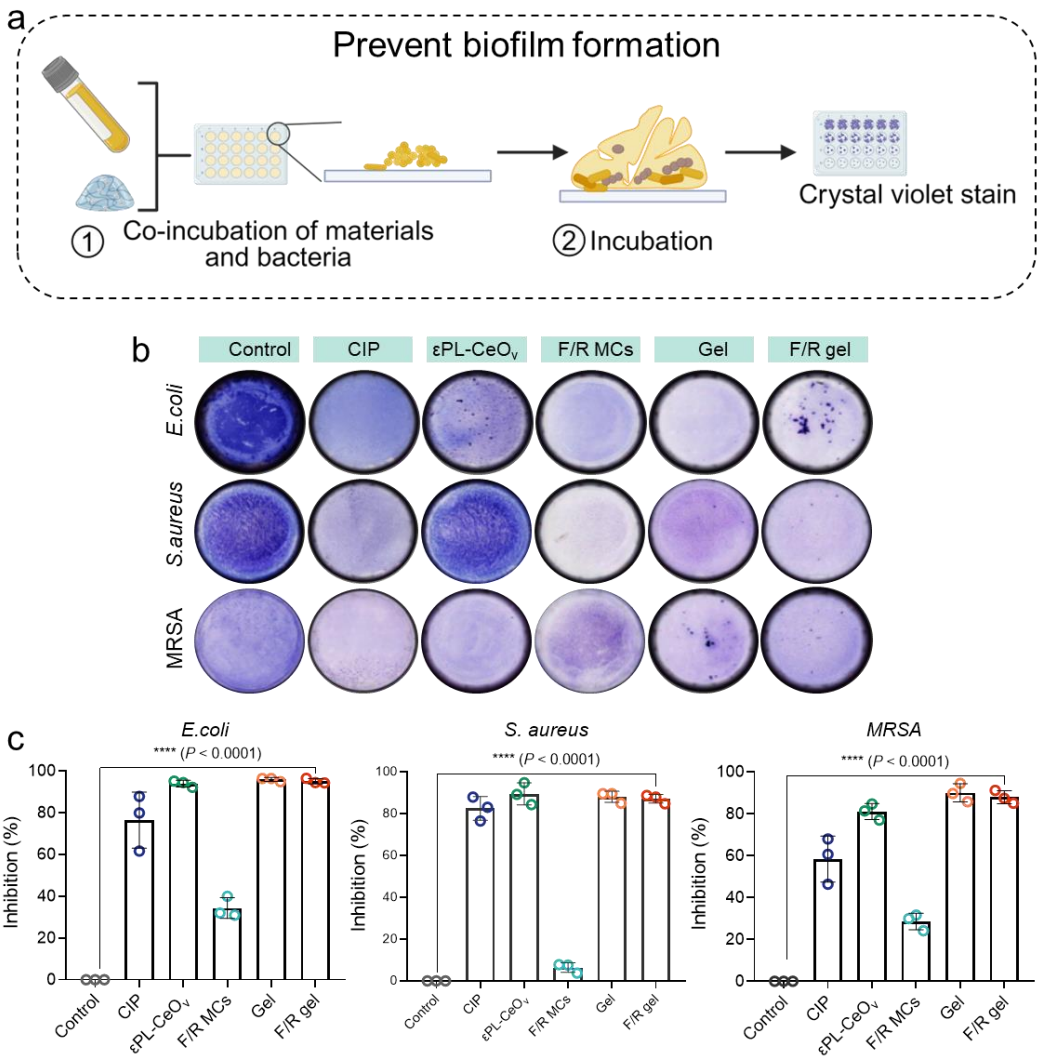

Supplementary Figure 22. Inhibition of biofilm formation by F/R gel (a) Experimental illustration of inhibiting biofilms by the F/R gel (created with BioRender.com). (b) Representative images of crystal violet staining for inhibiting biofilms. (c) Biofilm inhibition rate of the different samples on *E. coli*, *S. aureus*, and *MRSA* (n = 3 independent samples). Three independent experiments were performed and representative results are shown in (b). Data are presented as mean ± SD and statistical significance was analyzed via one-way ANOVA with Tukey's multiple comparison test. *P* value: **P* < 0.05, ***P* < 0.01, ****P* < 0.001, *****P* < 0.0001.

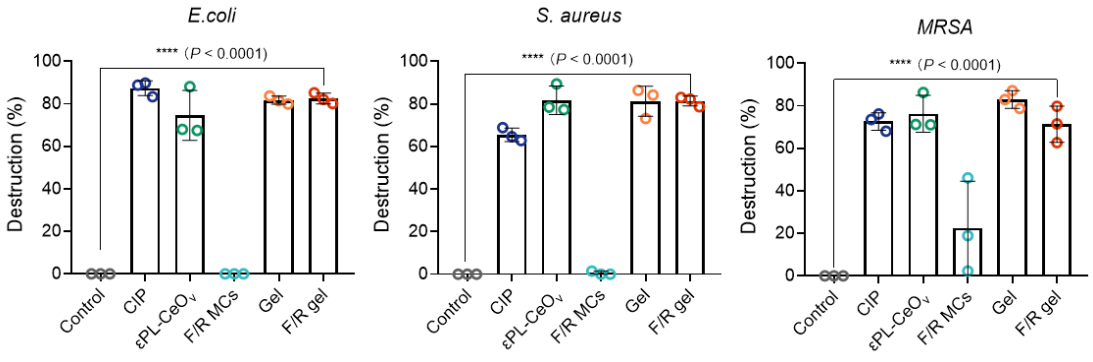

Supplementary Figure 23. Biofilm destruction rate of the different samples on *E. coli*, *S. aureus*, and *MRSA* (n = 3 independent samples).

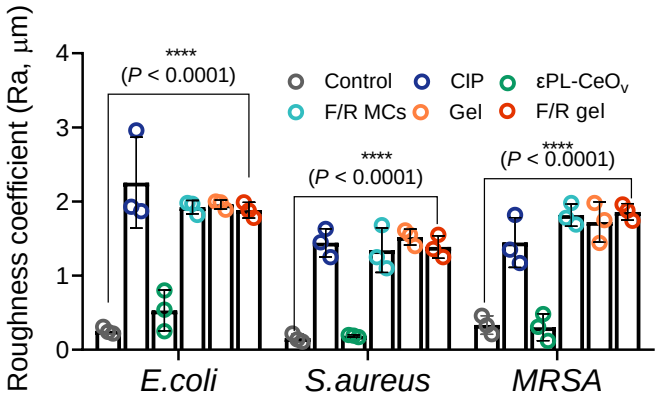

Supplementary Figure 24. Roughness analysis of the treated biofilms by image J (n = 3 independent samples).

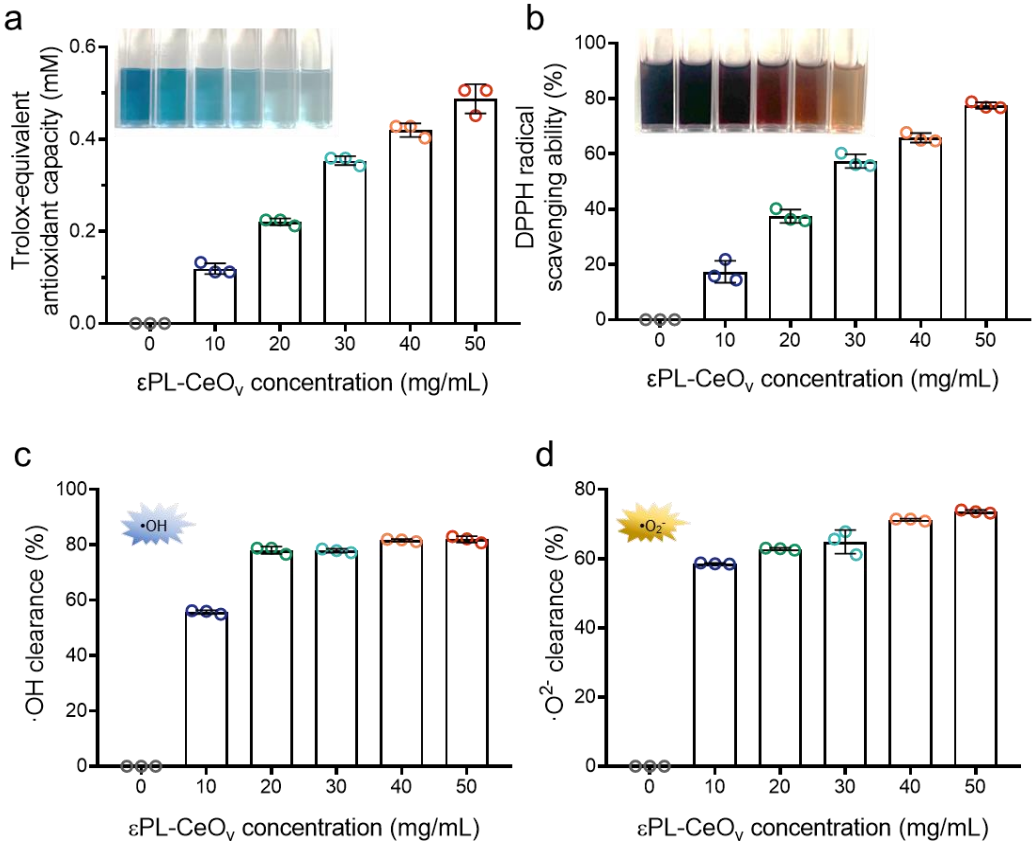

Supplementary Figure 25. The ability of εPL-CeO_v nanoparticles to scavenge (a) $ABTS^{+}$•, (b) DPPH•, (c) •OH, and (d) $•O_2^-$ (n = 3 independent samples).

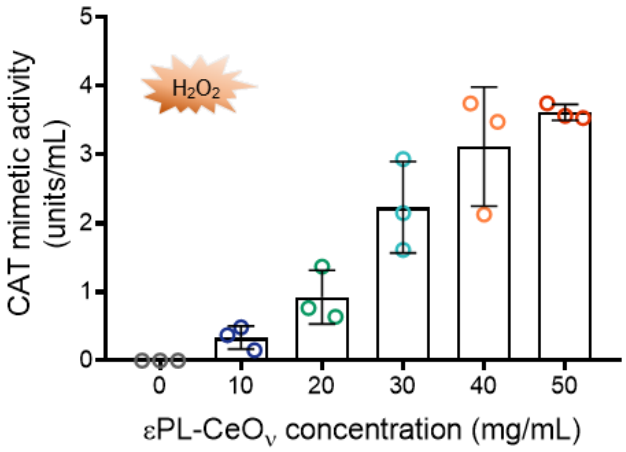

Supplementary Figure 26. CAT-mimetic activity of the εPL-CeO_v nanoparticles (n = 3 independent samples).

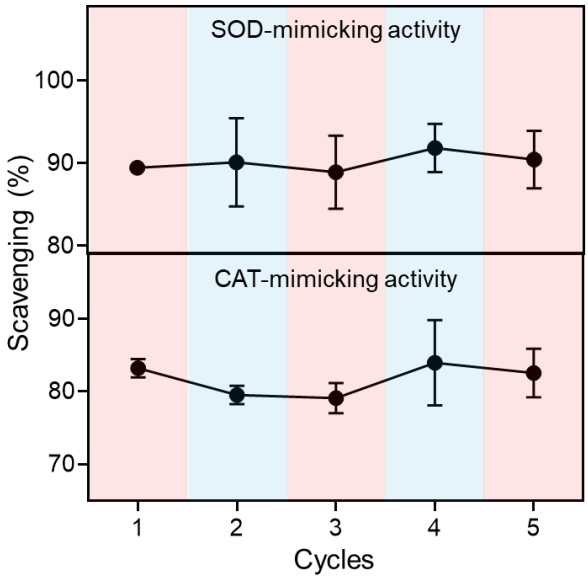

Supplementary Figure 27. ROS scavenging stability test of εPL-CeO_v nanoparticles during 5 cycles (n = 3 independent samples).

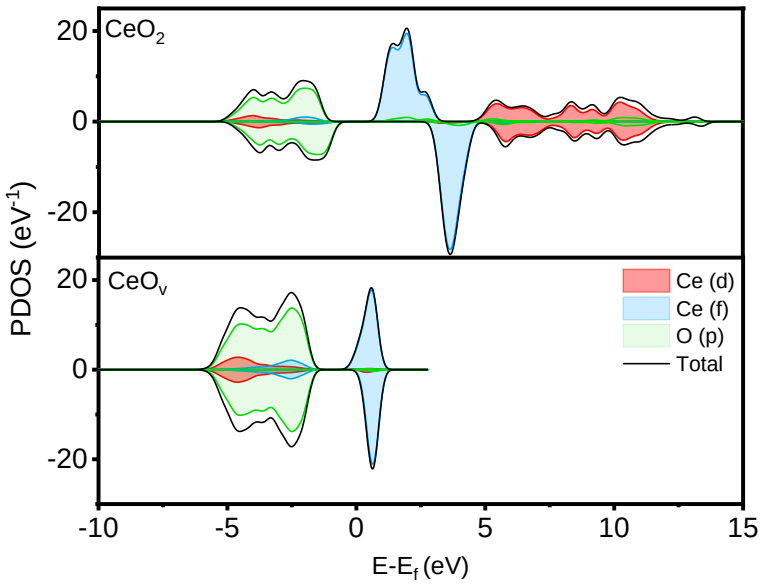

Supplementary Figure 28. PDOS profiles of CeO_2 (upper panel) and CeO_v (bottom panel). Energy at E = 0 eV represents the Fermi energy.

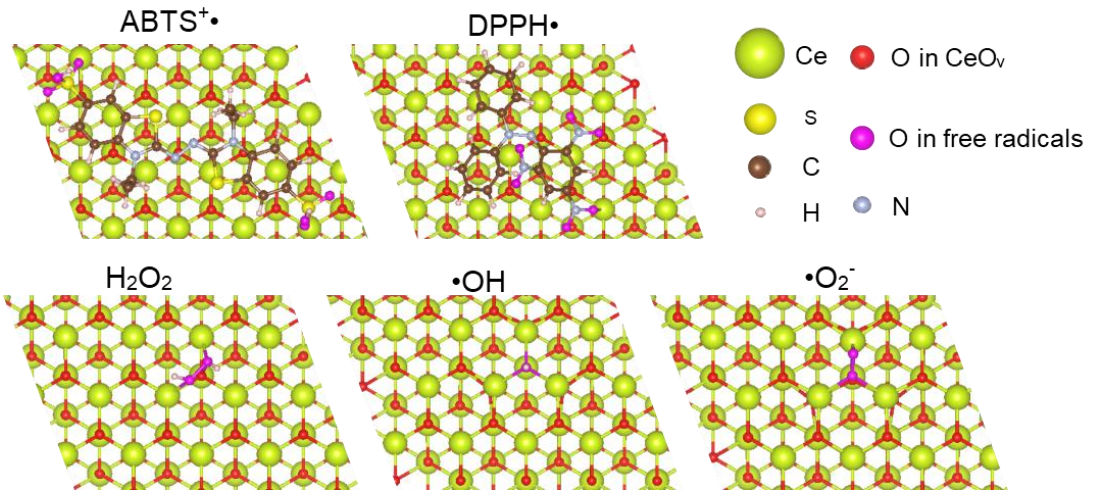

Supplementary Figure 29. Top view for the optimized structures of $ABTS^{+}$•, DPPH•, H_2O_2, •OH, and $•O_2^-$ free radicals adsorbed on CeO_2 (111) facets.

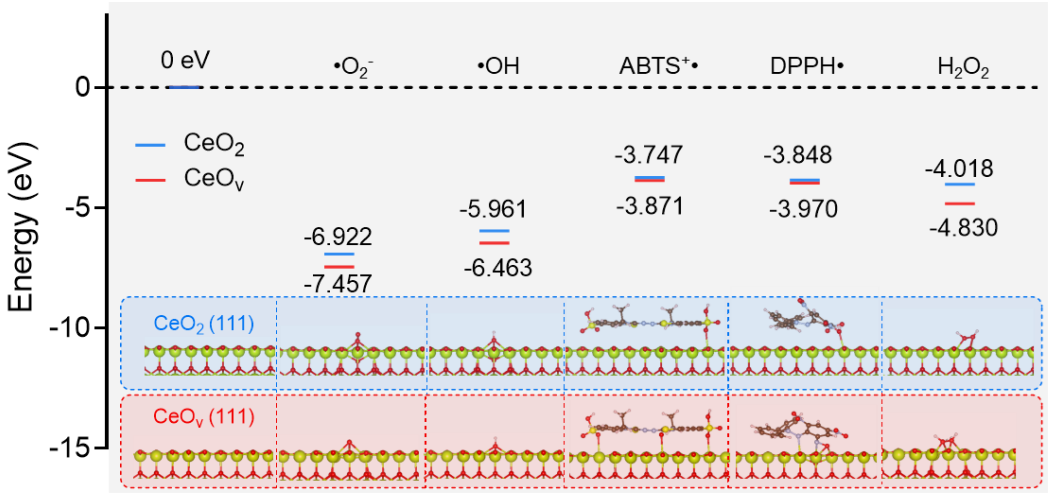

Supplementary Figure 30. Binding energy of different free radical units adsorbed on CeO_2 (111) and CeO_v (111) facets. The segment adsorption models are shown at the bottom.

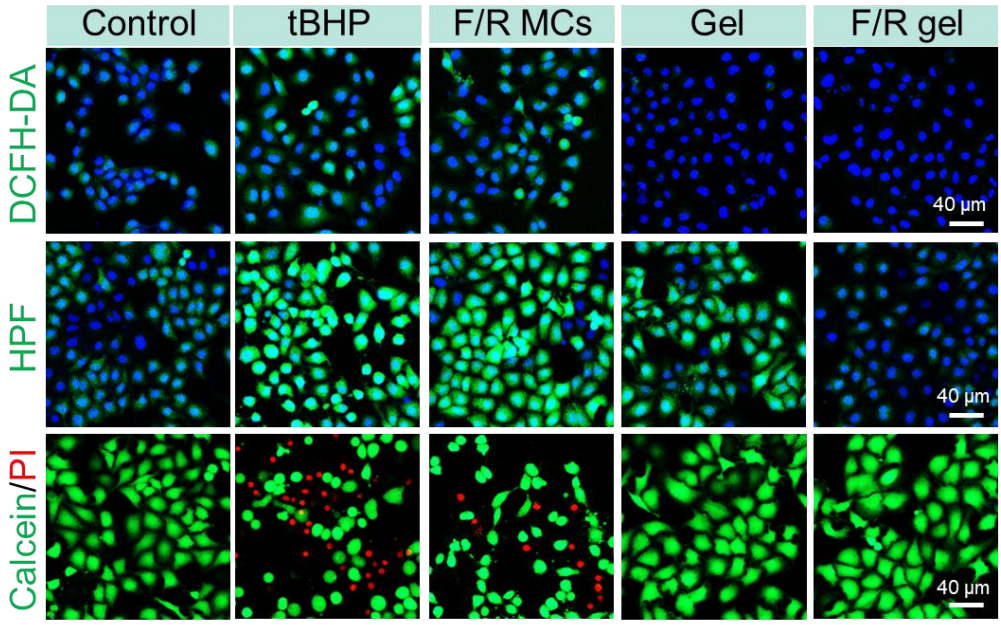

Supplementary Figure 31. DCFH-DA fluorescence, HPF fluorescence and live/dead cell staining images of HUVECs in the different groups. Three independent experiments were performed and representative results are shown.

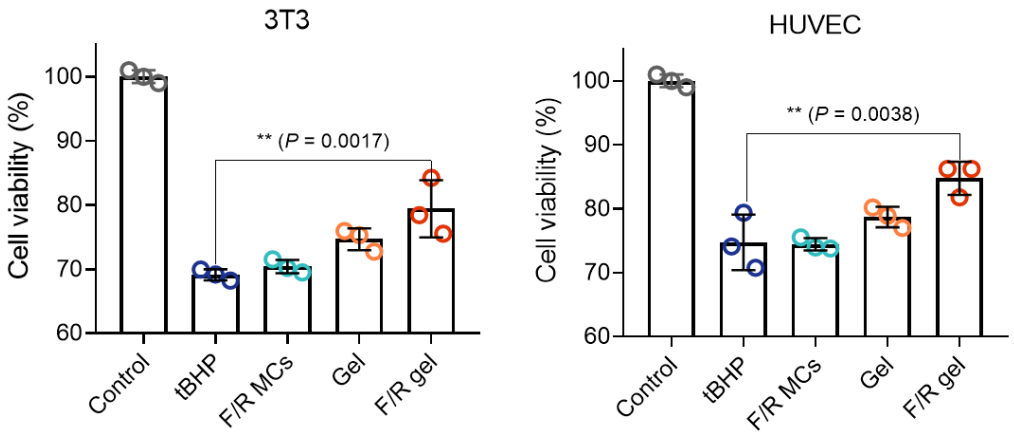

Supplementary Figure 32. Cell viability of 3T3 and HUVEC upon the different treatments. Data are presented as mean ± SD and statistical significance was analyzed via one-way ANOVA with Tukey's multiple comparison test. *P* value: **P* < 0.05, ***P* < 0.01, ****P* < 0.001, *****P* < 0.0001.

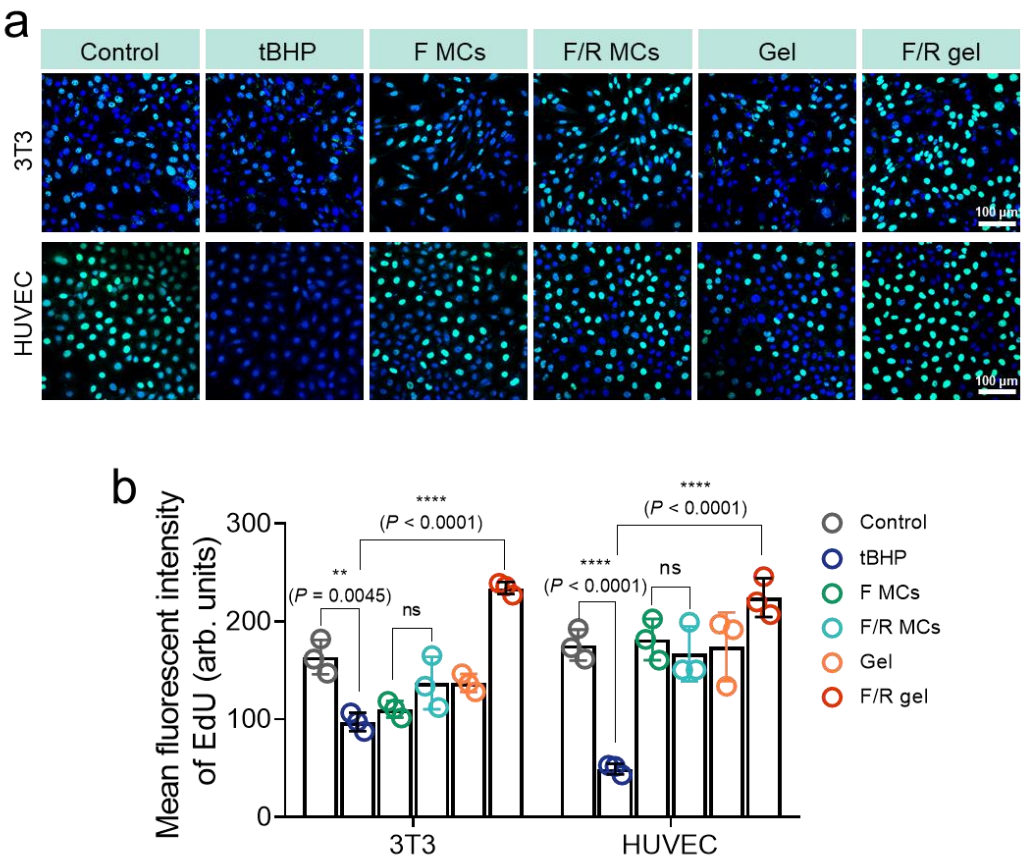

Supplementary Figure 33. F/R gel promotes cell proliferation (a) Fluorescence images of cellular EdU staining assay on 3T3 cells and HUVECs. (b) The corresponding statistical analysis (n = 3). Data are presented as mean ± SD and statistical significance was analyzed via one-way ANOVA with Tukey's multiple comparison test. *P* value: **P* < 0.05, ***P* < 0.01, ****P* < 0.001, *****P* < 0.0001.

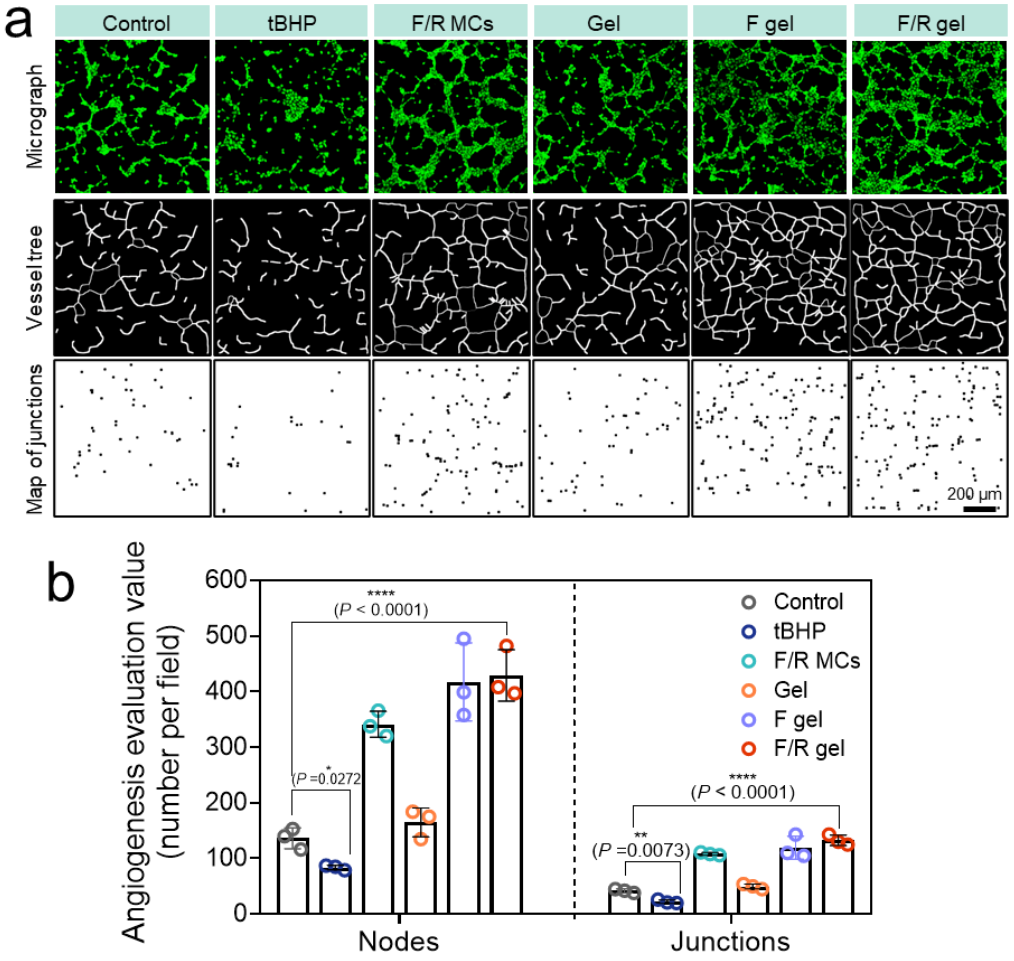

Supplementary Figure 34. Tube formation in HUVECs after tBHP stimulation followed by F/R treatment of cells. (a) Representative images of the cells and Vessel tree and map of junctions analyzed by image J. (b) Statistical data for Nodes and Junctions (n = 3 independent samples). Data are presented as mean ± SD and statistical significance was analyzed via one-way ANOVA with Tukey's multiple comparison test. *P* value: **P* < 0.05, ***P* < 0.01, ****P* < 0.001, *****P* < 0.0001.

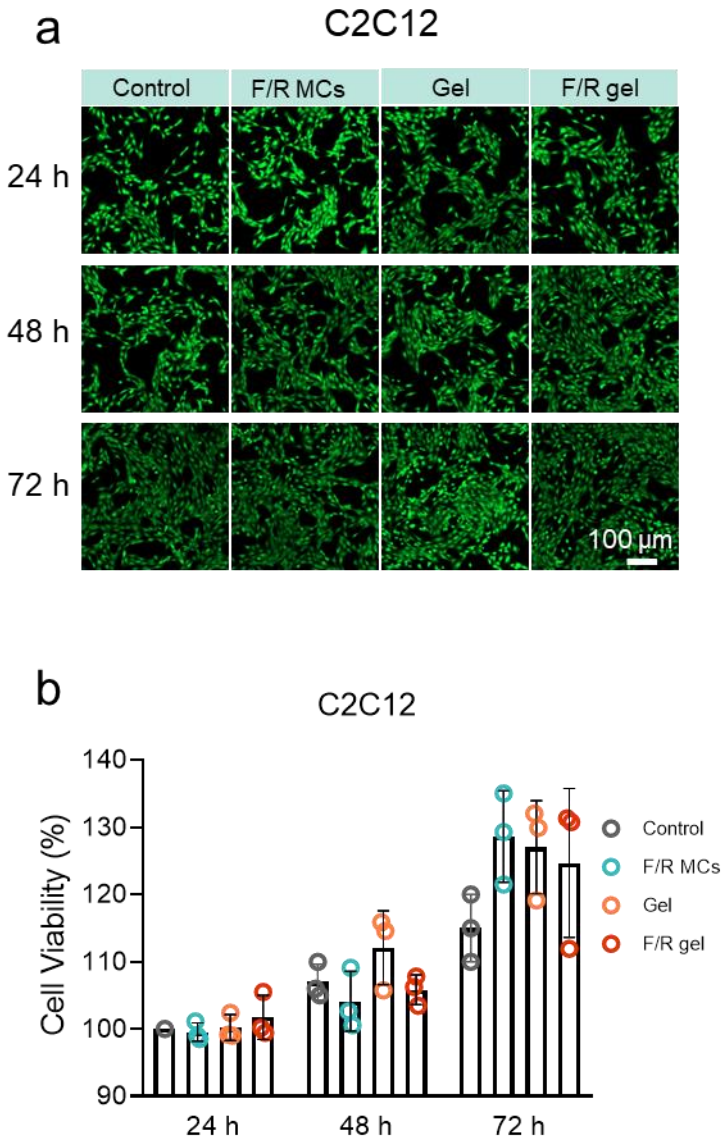

Supplementary Figure 35. Live/dead cell staining images and cell viability (n = 3 independent samples) of C2C12 cells upon the different treatments. Data are presented as mean ± SD and statistical significance was analyzed via one-way ANOVA with Tukey's multiple comparison test. *P* value: **P* < 0.05, ***P* < 0.01, ****P* < 0.001, *****P* < 0.0001.

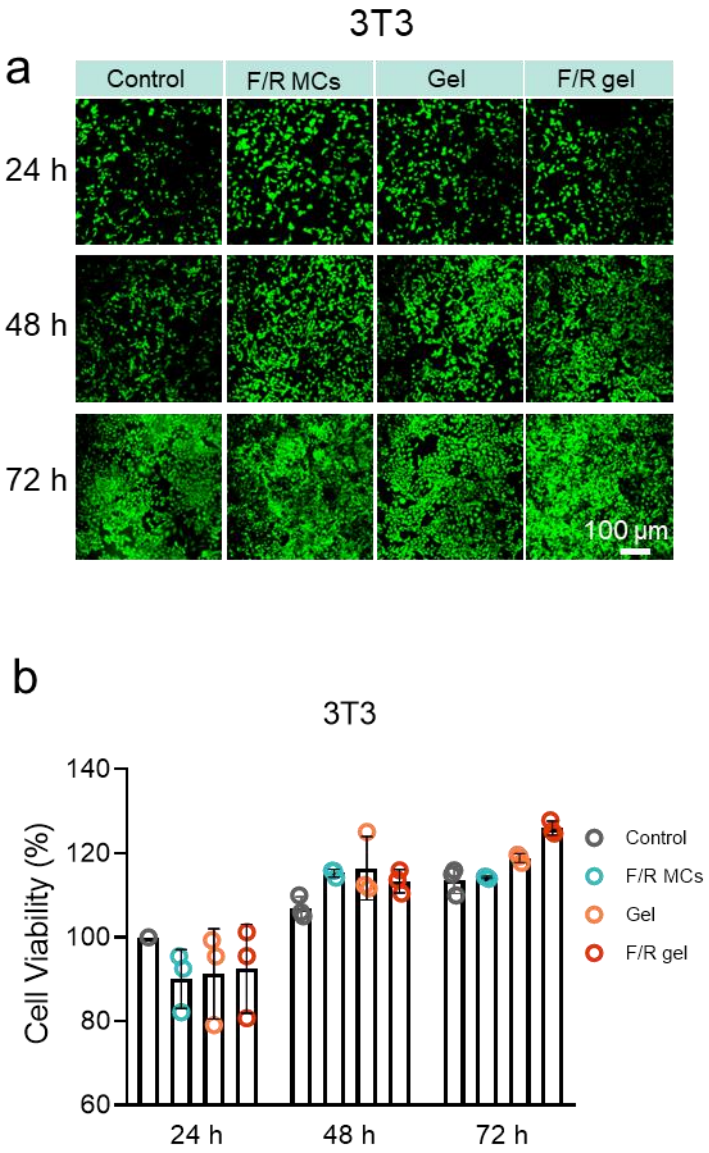

Supplementary Figure 36. Live/dead cell staining images and cell viability (n = 3 independent samples) of 3T3 upon the different treatments. Data are presented as mean ± SD and statistical significance was analyzed via one-way ANOVA with Tukey's multiple comparison test. *P* value: **P* < 0.05, ***P* < 0.01, ****P* < 0.001, *****P* < 0.0001.

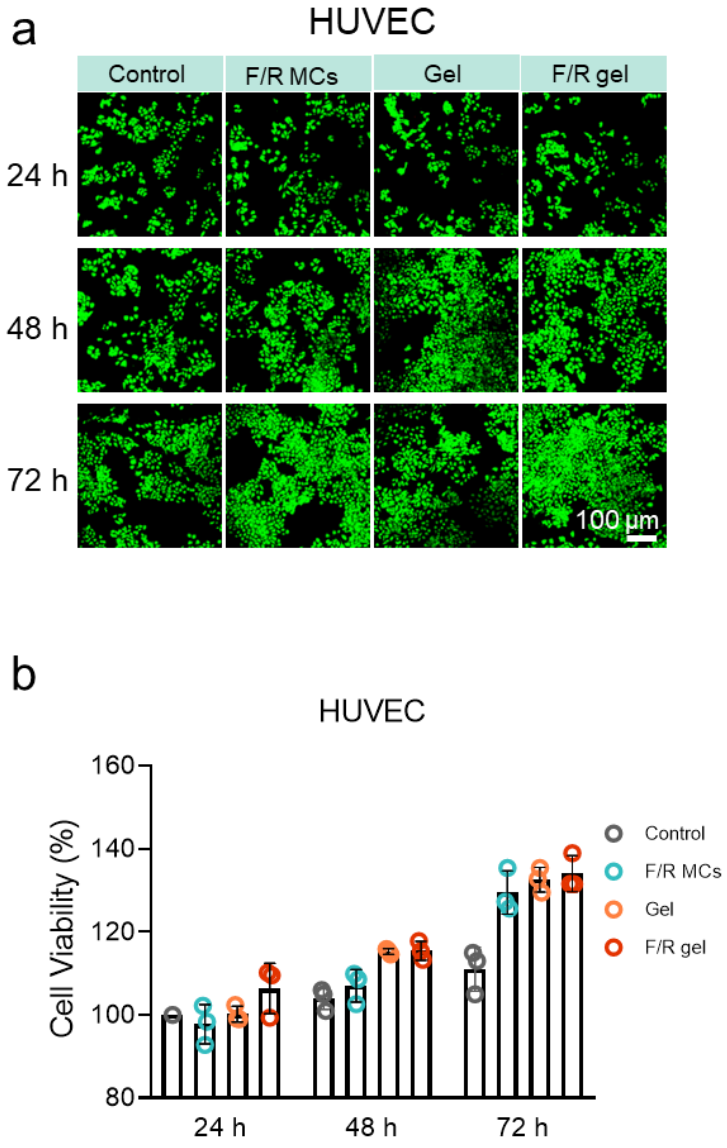

Supplementary Figure 37. Live/dead cell staining images and cell viability (n = 3 independent samples) of HUVEC upon the different treatments. Data are presented as mean ± SD and statistical significance was analyzed via one-way ANOVA with Tukey's multiple comparison test. *P* value: **P* < 0.05, ***P* < 0.01, ****P* < 0.001, *****P* < 0.0001.

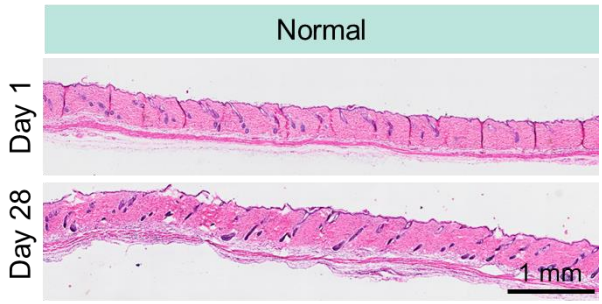

Supplementary Figure 38. H&E staining images of normal skin. Three independent experiments were performed and representative results are shown.

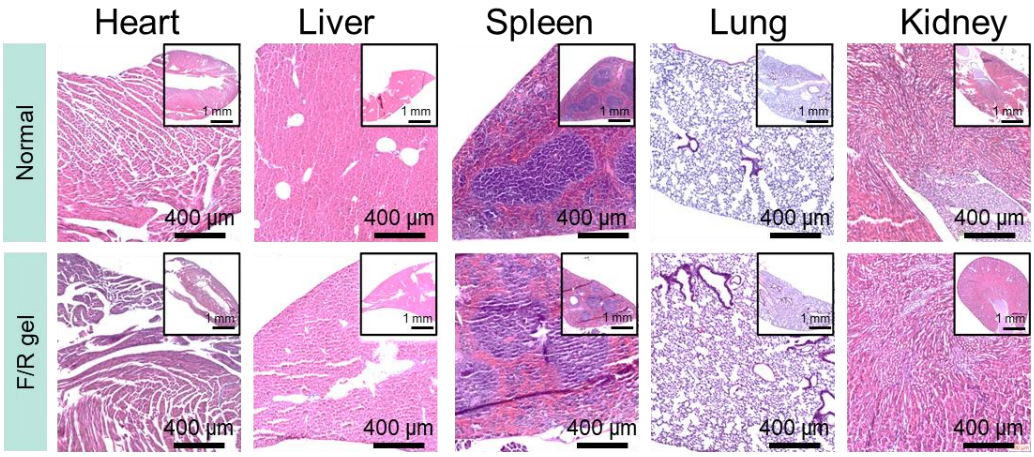

Supplementary Figure 39. H&E staining images of the major organs after subcutaneous implantation experiment. Three independent experiments were performed and representative results are shown.

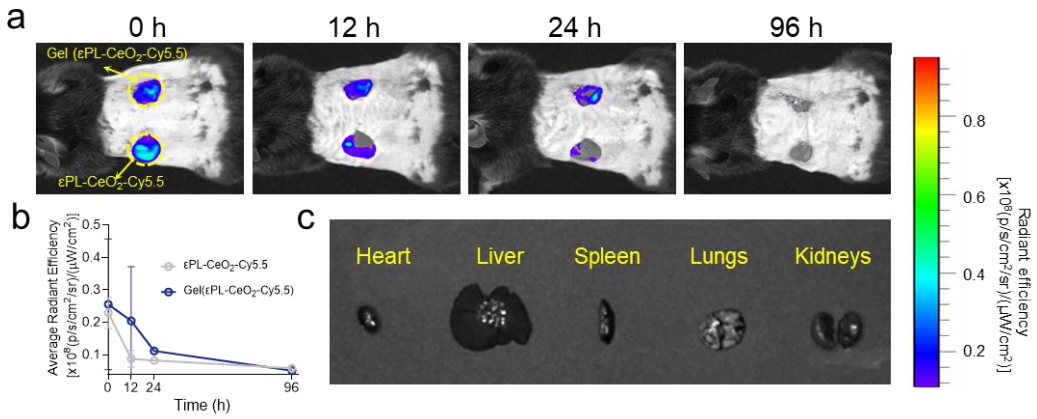

Supplementary Figure 40. Retention effect of εPL-CeO_v at the wound sites. (a) Representative images of εPL-CeO_v-Cy5.5 and Gel (εPL-CeO_v-Cy5.5) in mouse wounds at different time points. (b) Average radiant efficiency of mouse wound sites at different time points (n = 3 biologically independent samples). (c) Representative images of fluorescence intensity in the isolated tissues at 96 h. Three independent experiments were performed and representative results are shown in a, c. Data are presented as mean ± SD and statistical significance was analyzed via two-way ANOVA with Tukey's multiple comparison test. *P* value: **P* < 0.05, ***P* < 0.01, ****P* < 0.001, *****P* < 0.0001.

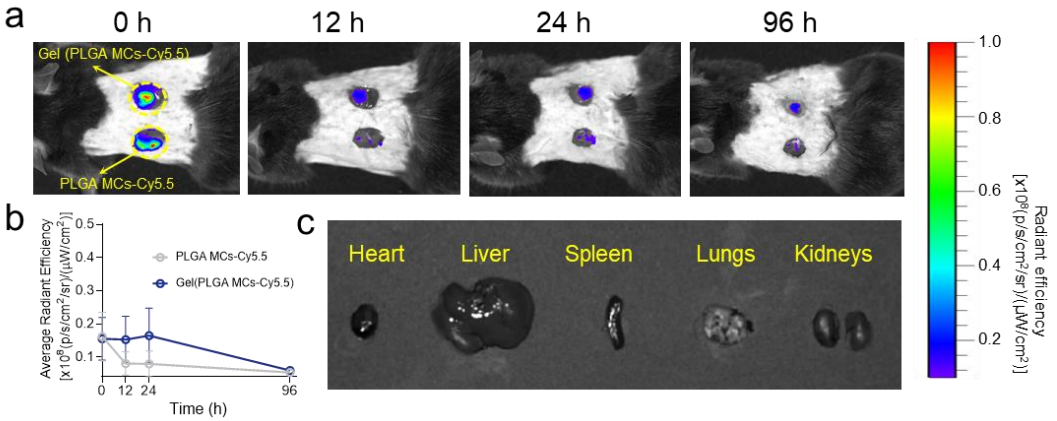

Supplementary Figure 41. Retention experiments of PLGA MCs-Cy5.5 at the wound site. (a) Representative images of PLGA MCs-Cy5.5 and Gel (PLGA MCs-Cy5.5) in mouse wound areas at different time points. (b) Representative images of fluorescence intensity in the isolated tissues at 96 h. (c) Average radiant efficiency of mouse wound sites at different time points (n = 3 biologically independent samples). Three independent experiments were performed and representative results are shown in a, c. Data are presented as mean ± SD and statistical significance was analyzed via two-way ANOVA with Tukey's multiple comparison test. *P* value: **P* < 0.05, ***P* < 0.01, ****P* < 0.001, *****P* < 0.0001.

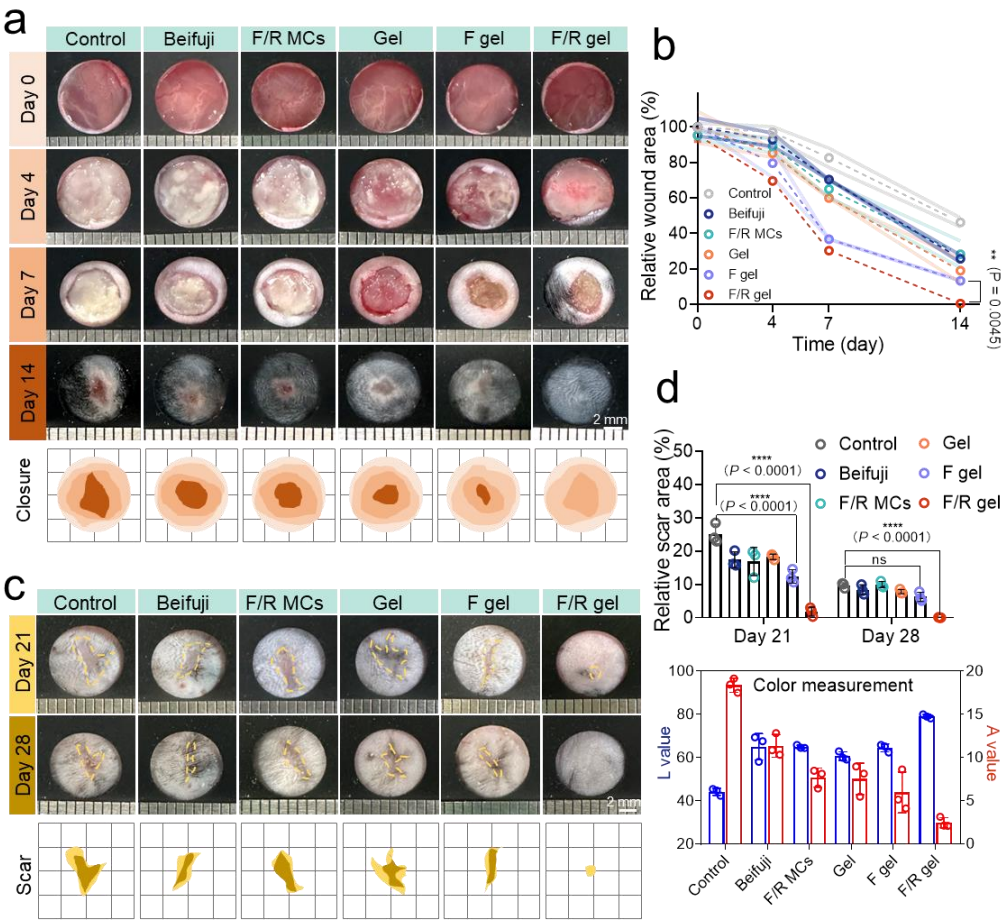

Supplementary Figure 42. Wound healing efficacies of F/R gel in mice. (a) Optical photos and simulated graphs of wound closure changes from day 0 to day 14. (b) Variation curve of wound areas within 14 days (n = 3 biologically independent samples). (c) Optical photos and simulated graphs of scar area changes from day 21 to 28. (d) Scar changing curve and color analysis of scar tissues post-treatments (a higher L value represents a whiter color, and a higher A value represents a redder color) (n = 3 biologically independent samples). Three independent experiments were performed and representative results are shown in a-d. Data are presented as mean ± SD and statistical significance was analyzed via two-way ANOVA with Tukey's multiple comparison test. *P* value: **P* < 0.05, ***P* < 0.01, ****P* < 0.001, *****P* < 0.0001.

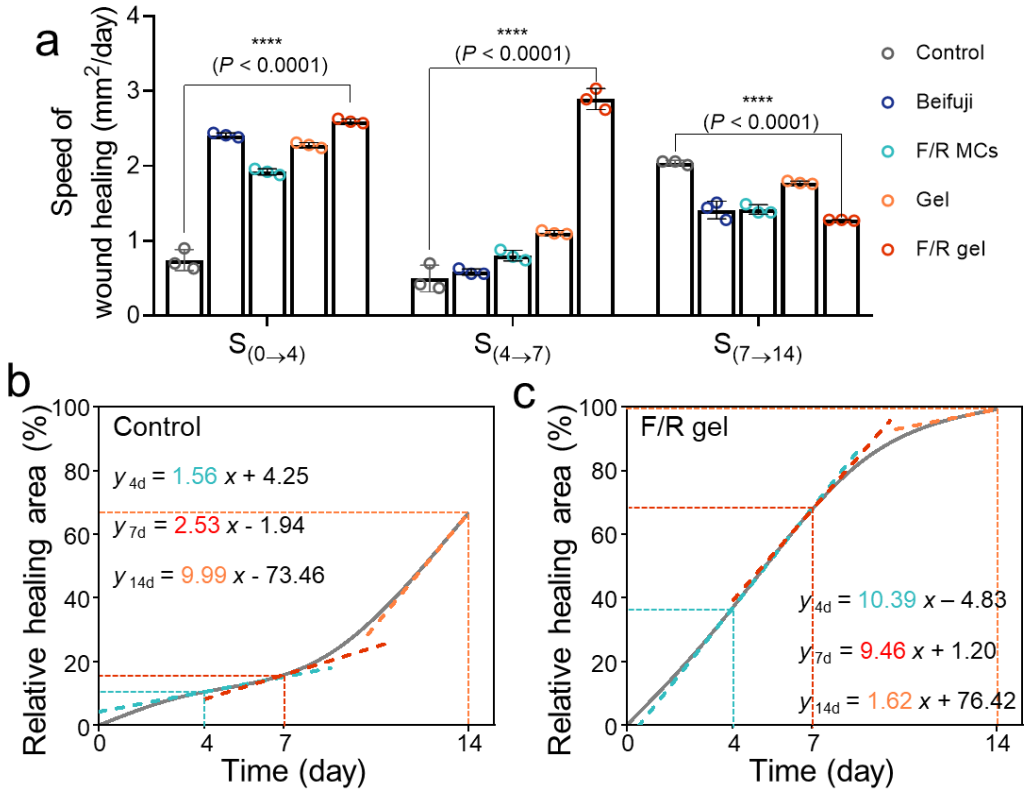

Supplementary Figure 43. Characterization of the rate of wound healing promoted by F/R gel (a) Average speed of repair at each stage of wound healing (n = 3 biologically independent samples). Fitted curves of healing efficiency for the (b) Control and (c) F/R groups, where the tangent lines reflect the speed of wound repair at different phases. Data are presented as mean ± SD and statistical significance was analyzed via two-way ANOVA with Tukey's multiple comparison test. *P* value: **P* < 0.05, ***P* < 0.01, ****P* < 0.001, *****P* < 0.0001.

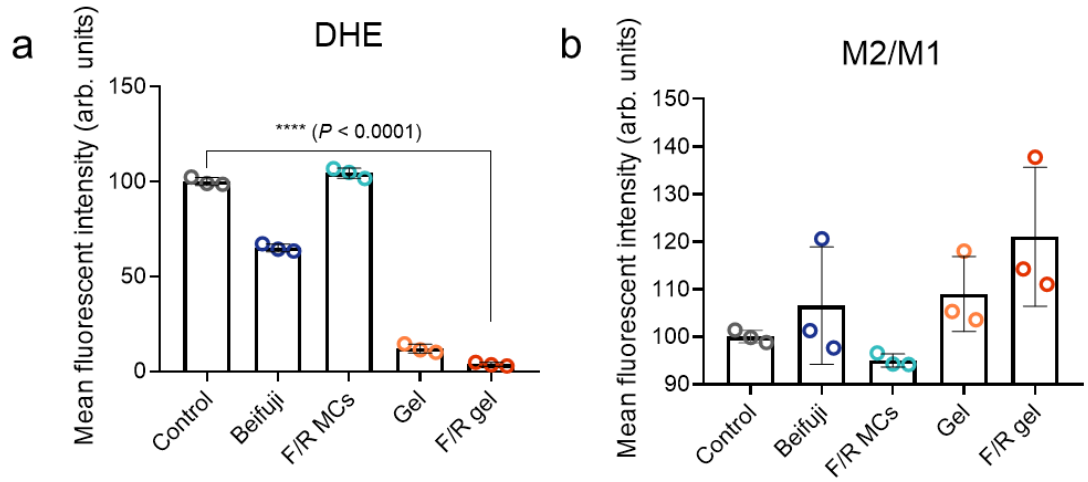

Supplementary Figure 44. Quantitative expression levels of (a) DHE staining and (b) M2/M1 ratios at the wound site on day 4. Data are presented as mean ± SD and statistical significance was analyzed via one-way ANOVA with Tukey's multiple comparison test. *P* value: **P* < 0.05, ***P* < 0.01, ****P* < 0.001, *****P* < 0.0001.

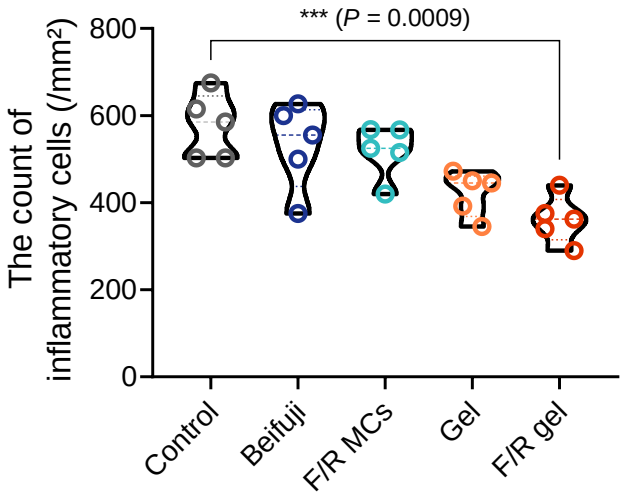

Supplementary Figure 45. The count of inflammatory cells at the wound site on day 7. Data are presented as mean ± SD and statistical significance was analyzed via one-way ANOVA with Tukey's multiple comparison test. *P* value: **P* < 0.05, ***P* < 0.01, ****P* < 0.001, *****P* < 0.0001.

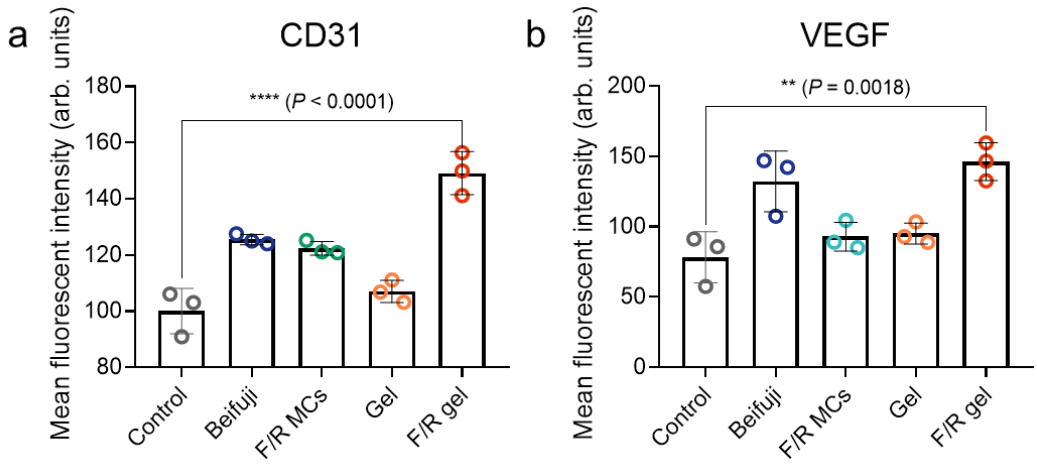

Supplementary Figure 46. Quantitative expression levels of (a) CD31 and (b)VEGF at the wound site on day 7. Data are presented as mean ± SD and statistical significance was analyzed via two-way ANOVA with Tukey's multiple comparison test. *P* value: **P* < 0.05, ***P* < 0.01, ****P* < 0.001, *****P* < 0.0001.

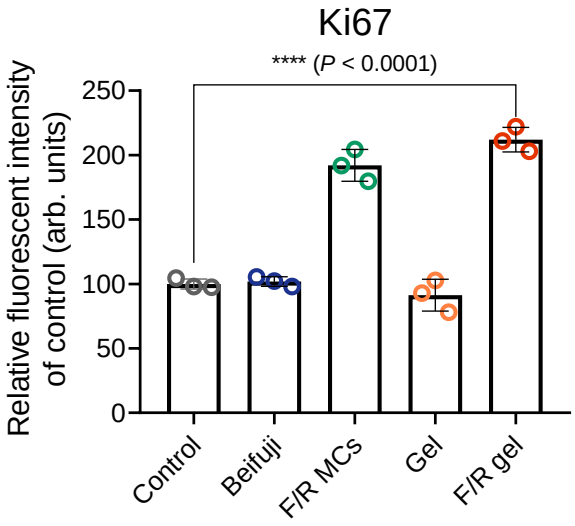

Supplementary Figure 47. Quantitative expression levels of Ki67 analyzed at the wound site on day 7. Data are presented as mean ± SD and statistical significance was analyzed via two-way ANOVA with Tukey's multiple comparison test. *P* value: **P* < 0.05, ***P* < 0.01, ****P* < 0.001, *****P* < 0.0001.

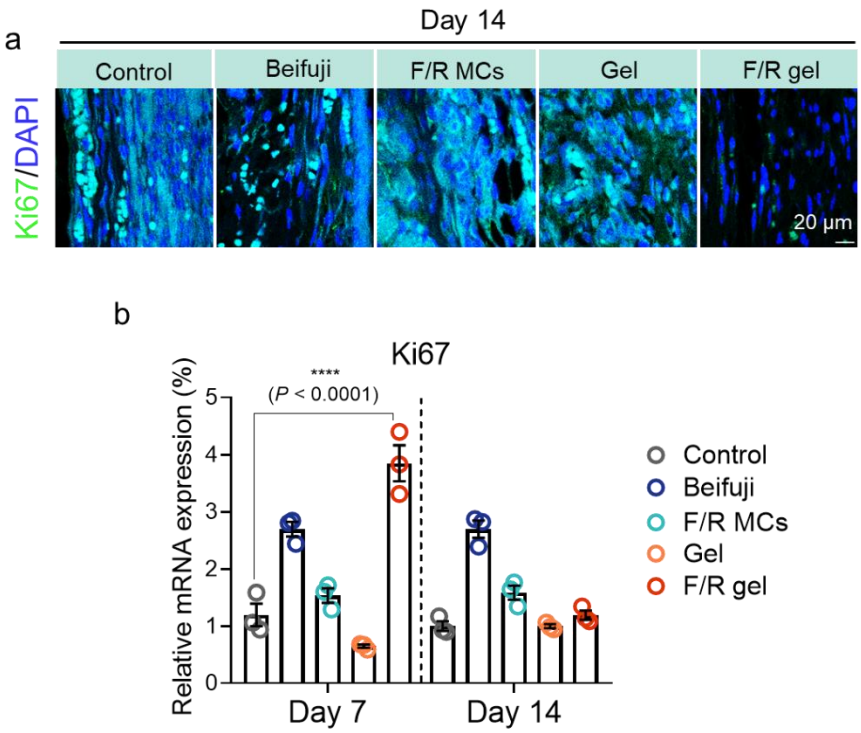

Supplementary Figure 48. Expression of Ki67 at different periods of wound. (a) Immunofluorescence staining images of Ki67 in the skin tissues on day 14. (b) Relative mRNA expressions of Ki67 in different groups on day 7 and day 14 (n = 3 independent samples). Three independent experiments were performed and representative results are shown in a. Data are presented as mean ± SD and statistical significance was analyzed via two-way ANOVA with Tukey's multiple comparison test. *P* value: **P* < 0.05, ***P* < 0.01, ****P* < 0.001, *****P* < 0.0001.

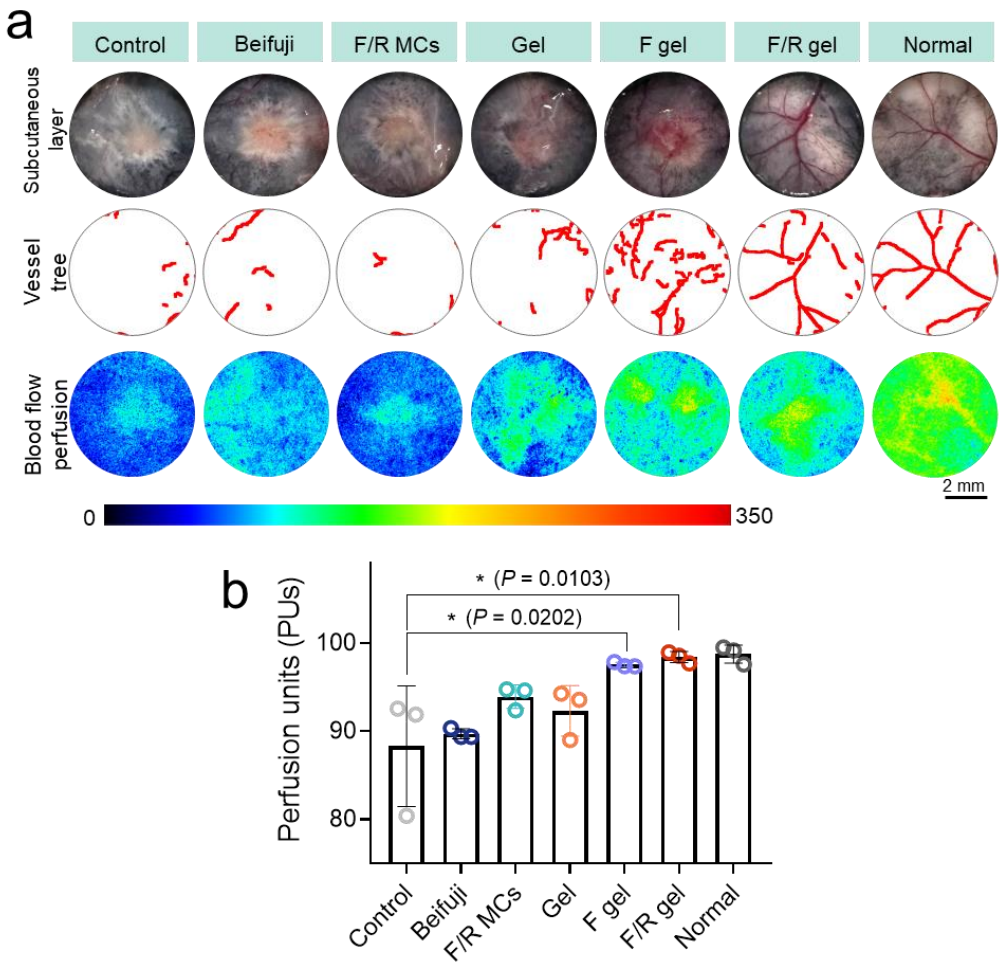

Supplementary Figure 49. Effects of F/R gel on angiogenesis. (a) The new blood vessels on subcutaneous layer of wound site, vessel tree analyzed by image J and blood flow perfusion of the wound site on day 14. (b) Statistical results of Blood flow perfusion (n = 3 biologically independent samples). Data are presented as mean ± SD and statistical significance was analyzed via one-way ANOVA with Tukey's multiple comparison test. P value: *$P < 0.05$, **$P < 0.01$, ***$P < 0.001$, ****$P < 0.0001$.

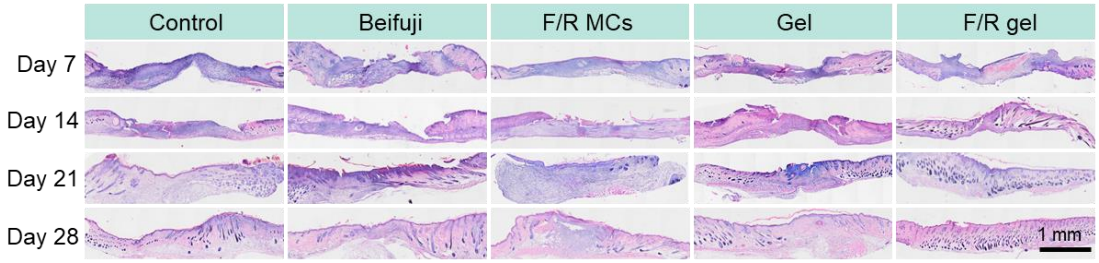

Supplementary Figure 50. H&E staining images of the wound sites in MRSA-infected mice chronic wounds model. Three independent experiments were performed and representative results are shown.

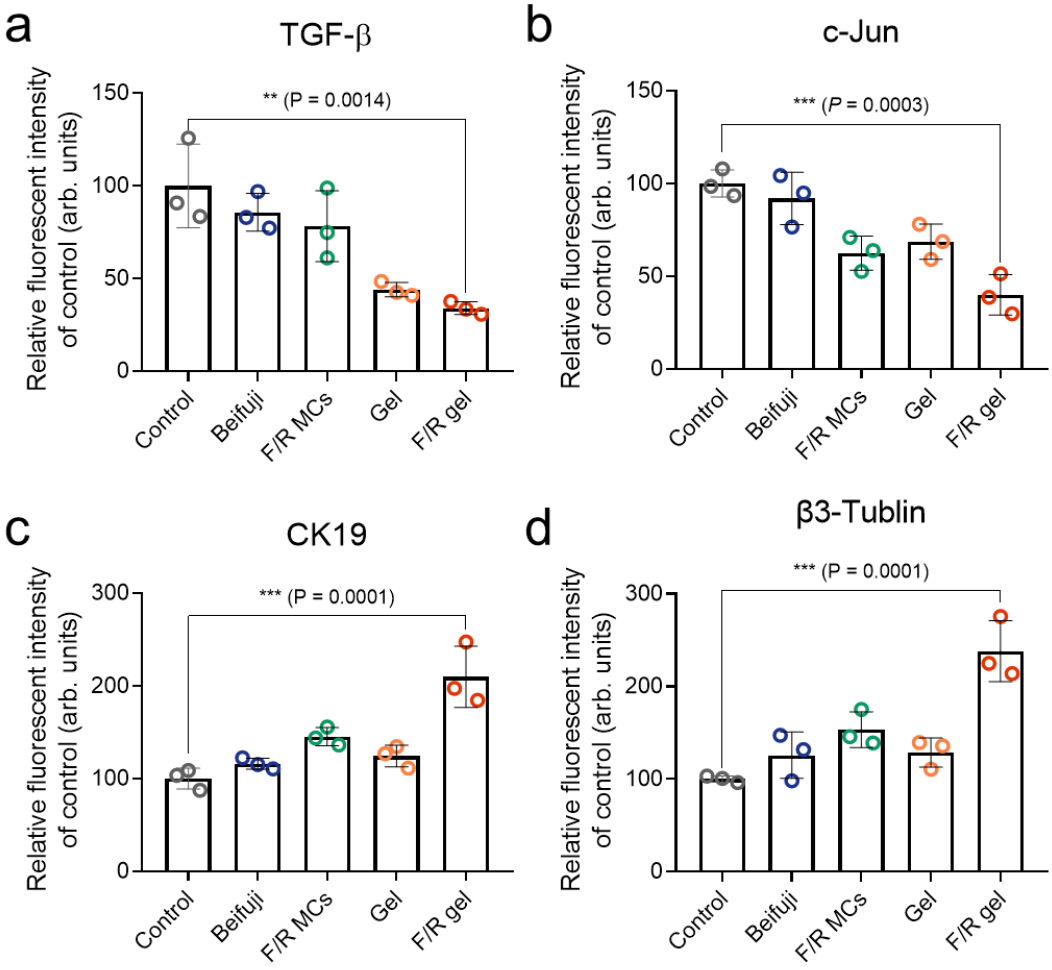

Supplementary Figure 51. Quantitative expression levels of (a) TGF-β, (b) VEGF, (c) CK19 and(d) β3-Tublin at the wound site on day 28 (n = 3 biologically independent samples).

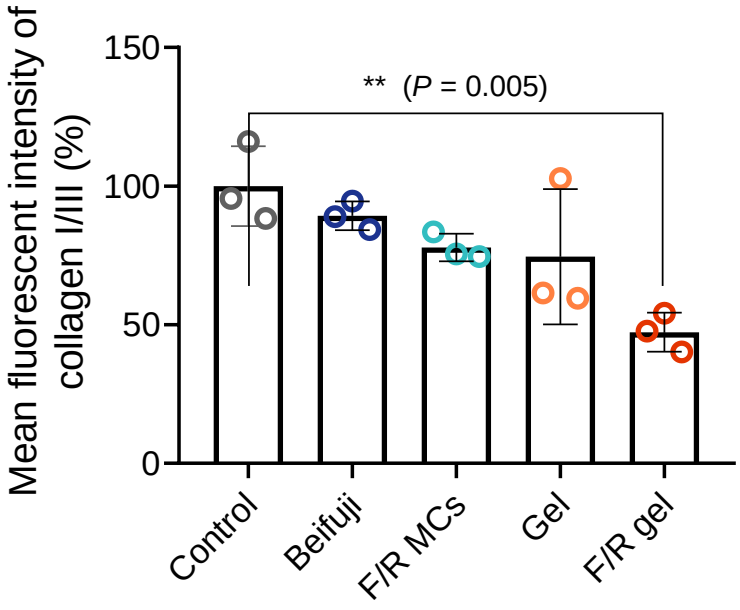

Supplementary Figure 52. Quantitative expression levels of collagen I/III ratios analyzed at the wound site (n = 3 biologically independent samples).

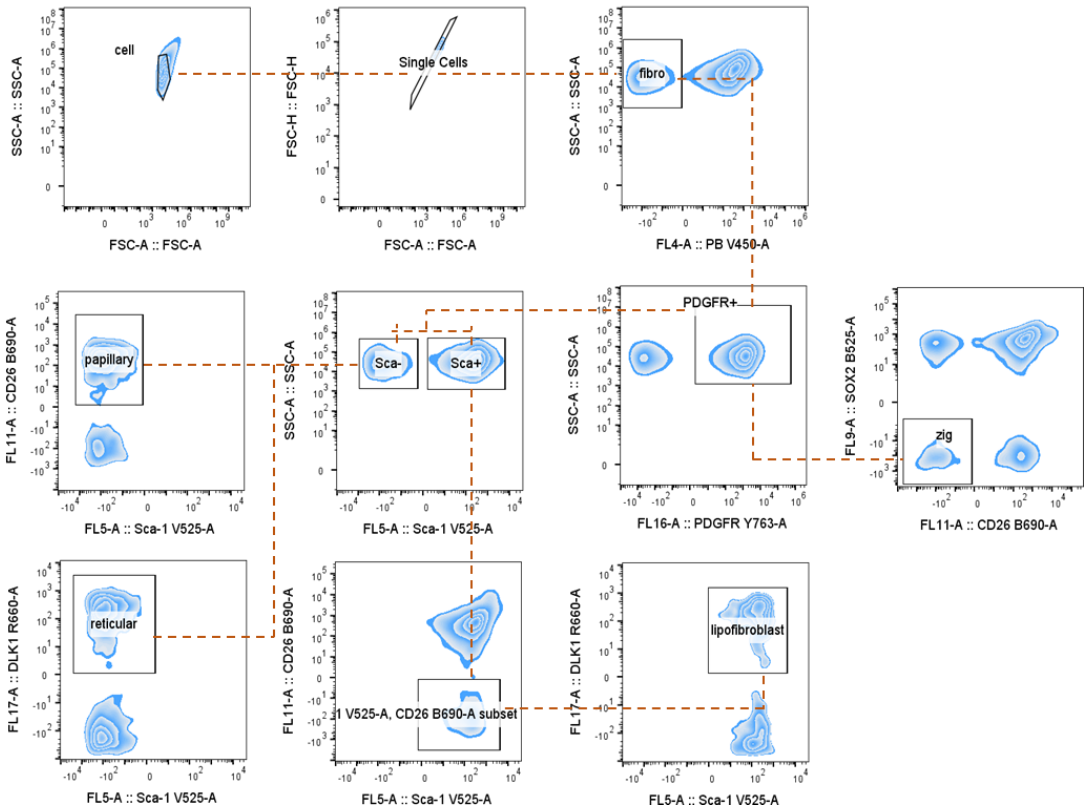

Supplementary Figure 53. Flow cytometry sorting experiments and gating strategies for the wound tissues.

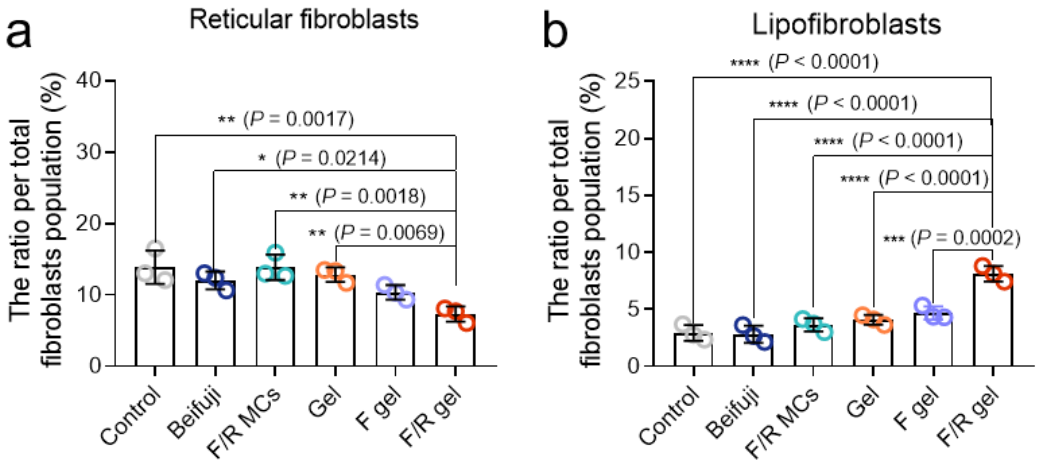

Supplementary Figure 54. Fluorescence-activated cell sorting results of fibroblast subtypes in wound tissues. (a)Reticular fibroblasts and (b) lipofibroblasts (n = 3 biologically independent samples).

Supplementary Table 1. Antibody information for immunofluorescence staining

Antibody name	Manufacturer	Catalog
CD86 Rabbit pAb	ABclonal	A16805
CD206 antibody	Proteintech	18704-1-AP
CD68 antibody	Proteintech	66231-2-Ig
Anti-CD31 antibody	abcam	ab32457
VEGFA Polyclonal antibody	Proteintech	19003-1-AP
Ki67 Antibody	Santa Cruz Biotechnology	sc-23900
Cytokeratin 10 Antibody	Santa Cruz Biotechnology	sc-23877
Anti-Collagen I antibody	abcam	ab138492
Anti-Collagen III antibody	abcam	ab6310
Anti-TGFBI antibody	abcam	ab170874
Anti-c-jun antibody	abcam	ab31419
Cytokeratin 19 Monoclonal antibody	Proteintech	60187-1-Ig
Anti-beta III Tubulin antibody	abcam	ab18207
Anti-alpha smooth muscle Actin	abcam	ab7817
Ly6A Rabbit Monoclonal Antibody	Beyotime	AG5285

Supplementary Table 2. Primer sequences for RT-PCR

Primer name	Forward primer (5' to 3')	Reverse primer (5' to 3')
IL-1β	AAATGCCACCTTTTGACAGTG	TGGATGCTCTCATCAGGACAG
TNF-α	GAACACGTCGTGGGATAATG	GGCAGACTTTGGATGCTTCTT
CD86	TGTTTCCGTGGAGACGCAAG	TTGAGCCTTTGTAAATGGGCA
iNOS	TTCTCAGCCCAACAATACAAGA	GTGGACGGGTCGATGTCAC
Arg1	CTCCAAGCCAAAGTCCTTAGAG	GGAGCTGTCATTAGGGACATCA
CD206	CTGGGGTTCCATCACTCCAC	AATCAGTGGTGGCCCTATGC
IL-10	CTTACTGACTGGCATGAGGATCA	GCAGCTCTAGGAGCATGTGG
Ki67	ACACCACACAAGAGCAGGAG	CACTGTGATCTTCCAGCGGT
COL I	CATGTTCAGCTTTGTGGACCT	GCAGCTGACTTCAGGGATGT
COL III	TCCCCTGGAATCTGTGAATC	TGAGTCGAATTGGGGAGAAT
c-Jun	TGGGCACATCACCACTACAC	TCTGGCTATGCAGTTCAGCC
GAPDH	GTCAAGGCCGAGAATGGGAA	CTCGTGGTTCACACCCATCA

Supplementary Table 3. Antibody information for FACS experiment

Antibody name	Manufacturer	Catalog
Ter119-Pacific Blue	ThermoFisher Scientific	45-5921-82
CD45-PB	ThermoFisher Scientific	48-0451-82
CD31-PB	ThermoFisher Scientific	RM5228
CD324-Biotin	ThermoFisher Scientific	13-3249-82
CD202b-Biotin	ThermoFisher Scientific	13-5987-82
CD326-eFluor450	ThermoFisher Scientific	48-5791-82
CD26-PerCPCy5.5	ThermoFisher Scientific	45-0261-82
PDGFRα(CD140a)-PE-Cy7	ThermoFisher Scientific	25-1401-80
Sca-1(Ly-6A/E)-BV605	BioLegend	108133
PDGFRα-PE-Cy7	ThermoFisher Scientific	25-1401-82
DLK1-Allophycocyanin	R&D systems	FAB8634A
Streptavidin-eFluor450	ThermoFisher Scientific	48-4317-82

Supplementary Table 4. Reagent information for FACS experiment

Reagent name	Manufacturer	Catalog
collagenase IV	ThermoFisher Scientific	17104019
Hanks Buffered Salt Solution	solarbio	H1025
Fetal Bovine Serum	Gibco	10099-141
Penicillin-Streptomycin Solution	solarbio	P1400
Red Blood Cell Lysis Buffer	solarbio	R1010
DAPI	Beyotime	C1005

Supplementary Table 5. Comparison of recent key publications related to wound dressings in regenerative medicine and our work

Year	Form of wound dressing	Wound type	Therapeutic target	Accelerated wound closure	Inhibited scar formation	Ref.
2018	Nanotubes	Rabbit ear hypertrophic scar model	No clear target	Not mentioned	Yes	1
2021	Hydrogel	Rabbit ear hypertrophic scar model	Regulatory gene *Col1A1* for collagen deposition	Yes	Yes	2
2021	Hydrogel	Acute wound/Rabbit ear hypertrophic scar model	TGF - β signaling pathway	Yes	Yes	3
2021	Fiber	Acute wound	M2 macrophages	Yes	No	4
2021	Microneedle	Acute wound	Hypertrophic scar fibroblasts	Not mentioned	Yes	5
2022	Hydrogel	Diabetic wound	No clear target	Yes	No	6
2022	Hydrogel	Burn wound	No clear target	Yes	No	7
2022	Hydrogel	Acute wound	No clear target	Yes	No	8
2022	Intelligent bandage	Burn wound/ diabetic wound/S. aureus infected wound	No clear target	Yes	No	9
2023	Hydrogel	Diabetic wound	Macrophage	Yes	No	10
2023	Hydrogel	Diabetic wound	Macrophage	Not mentioned	No	11
2023	Hydrogel	Burn wound	No clear target	Yes	No	12
2023	Plaster patch	Acute wound	No clear target	Yes	No	13
2023	Wearable devices	*S. aureus* infected wound	No clear target	Yes	No	14
2023	Self-powered dressing	Burn wound /acute wound/*S. aureus* infected wound	No clear target	Yes	Yes	15
2023	Microneedle	Diabetic wound	No clear target	Yes	No	16

2023	Microneedle	Acute wound/*MRSA* infection wound/Rabbit ear hypertrophic scar model	Gene *Engrailed-1* in fibroblasts	Yes	Yes	17
2023	Microneedle patch	Diabetic wound	No clear target	Yes	No	18
2024	Hydrogel	*S. aureus* infected burn wound	No clear target	Yes	No	19
2024	Hydrogel	Diabetic wound	No clear target	Yes	No	20
2024	Hydrogel	*MRSA* infected wound	No clear target	Yes	No	21
2024	Hydrogel	S. aureus infected wound	No clear target	Yes	No	22
2024	Flexible conductive dressing	Acute wound	No clear target	Yes	No	23
2024	Intelligent bandage	Acute wound	No clear target	Yes	No	24
2024	Metal organic framework nanodots	Rabbit ear hypertrophic scar model	Fibroblast membranes within hypertrophic scar	Yes	No	25
2024	Hydrogel	*S. aureus* infected diabetic wound	No clear target	Yes	No	26
Our work	Hydrogel	*MRSA*-infected chronic wound/MRSA-infected rabbit ear hypertrophic scar wound model	*c-Jun* gene in fibroblasts	**Yes**, shorten wound closure time by about 1/3 compared with control group	**Yes**	

Supplementary References

1. Weng, W., *et al.* Aligned Carbon Nanotubes Reduce Hypertrophic Scar via Regulating Cell Behavior. *ACS Nano* **12**, 7601-7612 (2018).
2. Shen, Y., *et al.* Sequential Release of Small Extracellular Vesicles from Bilayered Thiolated Alginate/Polyethylene Glycol Diacrylate Hydrogels for Scarless Wound Healing. *ACS Nano* **15**, 6352-6368 (2021).
3. Zhang, J., *et al.* A pulsatile release platform based on photo-induced imine-crosslinking hydrogel promotes scarless wound healing. *Nat. Commun.* **12**, 1670 (2021).
4. Chen, L., *et al.* Programmable immune activating electrospun fibers for skin regeneration. *Bioact. Mater.* **6**, 3218-3230 (2021).
5. Wu, T., *et al.* Microneedle-Mediated Biomimetic Cyclodextrin Metal Organic Frameworks for Active Targeting and Treatment of Hypertrophic Scars. *ACS Nano* **15**, 20087-20104 (2021).
6. Shao, Z., *et al.* Wound microenvironment self-adaptive hydrogel with efficient angiogenesis for promoting diabetic wound healing. *Bioact. Mater.* **20**, 561-573 (2023).
7. Bakadia, B.M., *et al.* Biodegradable and injectable poly(vinyl alcohol) microspheres in silk sericin-based hydrogel for the controlled release of antimicrobials: application to deep full-thickness burn wound healing. *Adv. Compos. Hybrid Mater.* **5**, 2847-2872 (2022).
8. Liang, Y., *et al.* Bioinspired Injectable Self-Healing Hydrogel Sealant with Fault-Tolerant and Repeated Thermo-Responsive Adhesion for Sutureless Post-Wound-Closure and Wound Healing. *Nanomicro Lett.* **14**, 185 (2022).
9. Jiang, Y., *et al.* Wireless, closed-loop, smart bandage with integrated sensors and stimulators for advanced wound care and accelerated healing. *Nat. Biotechnol.* **41**, 652-662 (2023).
10. Xiong, Y., *et al.* A Whole-Course-Repair System Based on Neurogenesis-Angiogenesis Crosstalk and Macrophage Reprogramming Promotes Diabetic Wound Healing. *Adv. Mater.* **35**, e2212300 (2023).
11. Qi, X., *et al.* An Immunomodulatory Hydrogel by Hyperthermia-Assisted Self-Cascade Glucose Depletion and ROS Scavenging for Diabetic Foot Ulcer Wound Therapeutics. *Adv. Mater.* **35**, e2306632 (2023).
12. Lan, J., *et al.* A Rapid Self-Pumping Organohydrogel Dressing with Hydrophilic Fractal Microchannels to Promote Burn Wound Healing. *Adv. Mater.* **35**, e2301765 (2023).
13. Lin, J., *et al.* Directional transport of drug droplets based on structural and wettability gradients on antibacterial Janus wound plaster with hemostatic, antiextravasation, and prehealing properties. *Adv. Compos. Hybrid Mater.* **6**, 193 (2023).
14. Ge, Z., *et al.* Wireless and Closed-Loop Smart Dressing for Exudate Management and On-Demand Treatment of Chronic Wounds. *Adv. Mater.* **35**, e2304005 (2023).
15. Luo, R., *et al.* Reshaping the Endogenous Electric Field to Boost Wound Repair via Electrogenerative Dressing. *Adv. Mater.* **35**, e2208395 (2023).
16. Zhang, X., *et al.* Bioinspired Adaptable Indwelling Microneedles for Treatment of Diabetic Ulcers. *Adv. Mater.* **35**, e2210903 (2023).
17. Zhang, Y., *et al.* Scarless wound healing programmed by core-shell microneedles. *Nat. Commun.* **14**, 3431 (2023).

18. Wu, X., *et al.* Microfluidic Templated Stem Cell Spheroid Microneedles for Diabetic Wound Treatment. *Adv. Mater.* **35**, e2301064 (2023).
19. Zhao, M., *et al.* Stem Cell-Derived Nanovesicles Embedded in Dual-Layered Hydrogel for Programmed ROS Regulation and Comprehensive Tissue Regeneration in Burn Wound Healing. *Adv. Mater.* **36**, e2401369 (2024).
20. Xiao, W., *et al.* A Viscous-Biofluid Self-Pumping Organohydrogel Dressing to Accelerate Diabetic Wound Healing. *Adv. Mater.* **36**, e2401539 (2024).
21. Yang, Y., *et al.* Bacteria-responsive programmed self-activating antibacterial hydrogel to remodel regeneration microenvironment for infected wound healing. *Natl. Sci. Rev.* **11**, nwae044 (2024).
22. Wang, H., *et al.* A capacitive polypyrrole-wrapped carbon cloth/bacterial cellulose antibacterial dressing with electrical stimulation for infected wound healing. *Adv. Compos. Hybrid Mater.* **7**, 10 (2024).
23. Yang, S.-B., *et al.* Rapid and Scar Free Wound Repair by Using a Biologically Flexible and Conductive Dressing Under Electrical Stimulation. *Adv. Funct. Mater.*, 2403724 (2024).
24. Kang, M., *et al.* Self-Powered Electrical Bandage Based on Body-Coupled Energy Harvesting. *Adv. Mater.* **36**, e2402491 (2024).
25. Kong, T., *et al.* Cucumber-Derived Extracellular Vesicle-Functionalized Metal-Organic Frameworks for Enhanced Photodynamic Therapy of Hypertrophic Scars. *Adv. Funct. Mater.* **34**, 2400379 (2024).
26. Wang, Z., *et al.* The Unprecedented Biodegradable Polyzwitterion: A Removal-Free Patch for Accelerating Infected Diabetic Wound Healing. *Adv. Mater.* **36**, e2404297 (2024).